Title

Regulation of kinase activity by combined action of juxtamembrane and C-terminal regions of receptors

Authors

Chi-Chuan Lin[1], Lukasz Wieteska[1], Guillaume Poncet-Montange[2], Kin M. Suen[1], Stefan T. Arold[3,4], Zamal Ahmed[5], John E. Ladbury[1]*

Affiliations

1 School of Molecular and Cellular Biology, and Astbury Centre for Structural Molecular Biology, University of Leeds, Leeds, LS2 9JT, UK.

2 Center for the Development of Therapeutics, Broad Institute of MIT & Harvard, Cambridge, MA 02142, USA.

3 King Abdullah University of Science and Technology, Computational Bioscience Research Center, Division of Biological and Environmental Sciences and Engineering, Thuwal, 23955-6900, Saudi Arabia.

4 Centre de Biochimie Structurale, CNRS, INSERM, Université de Montpellier, 34090 Montpellier, France.

5 Department of Molecular and Cellular Oncology, University of Texas, MD Anderson Cancer Center, Houston TX 77030, USA.

*Corresponding author. Email: j.e.ladbury@leeds.ac.uk

Abstract

Despite the kinetically-favorable, ATP-rich intracellular environment, the mechanism by which receptor tyrosine kinases (RTKs) repress activation prior to extracellular stimulation is poorly understood. RTKs are activated through a precise sequence of phosphorylation reactions starting with a tyrosine on the activation loop (A-loop) of the intracellular kinase domain (KD). This forms an essential mono-phosphorylated 'active intermediate' state on the path to further phosphorylation of the receptor. We show that this state is subjected to stringent control imposed by the peripheral juxtamembrane (JM) and C-terminal tail (CT) regions. This entails interplay between the intermolecular interaction between JM with KD, which stabilizes the asymmetric active KD dimer, and the opposing intramolecular binding of CT to KD. A further control step is provided by the previously unobserved direct binding between JM and CT. Mutations in JM and CT sites that perturb regulation are found in numerous pathologies, revealing novel sites for potential pharmaceutical intervention.

Introduction

Receptor tyrosine kinases (RTKs) are membrane bound receptors that consist of an extracellular ligand binding domain, a single pass transmembrane region and a cytoplasmic region with kinase activity. Previously it was thought that the initiation of signaling of RTKs required ligand-induced dimerization, followed by a precise order of autophosphorylation on the kinase domain (*1*). However, an increasing number of studies have shown that, in the absence of ligand stimulation, many RTKs are able to self-associate into signaling incompetent dimers (*2–6*). Within the context of this unliganded state, the extent of phosphorylation on the kinase domain is restricted to a single tyrosine within the A-loop (*4, 7, 8*) with the exception of EGFR (*9*). This mono-phosphorylated 'active intermediate' state is the precursor to the subsequent phosphorylation of additional tyrosine residues. The tight regulation of the active intermediate RTKs in the absence of stimuli is a fundamental precept of numerous cellular outcomes including cell growth, motility, differentiation and metabolism upon ligand stimulation. Dysregulation of the active intermediate state can have devastating effects on ligand-independent signaling, leading to multiple pathologies including cancer, developmental abnormalities and metabolic disorders. Thus, stringent control is required to prevent spontaneous phosphorylation of RTKs within the kinetically favorable, ATP-rich intracellular environment.

Such control is exerted by intracellular amino acid sequences peripheral to KD, both within the juxtamembrane (JM), and the C-terminal tail (CT) regions of the receptor. The modus operandi of these regions varies across different receptors and can lead to both down- and up-regulation of kinase activity (*10*). Structural studies, which have focused largely on the unphosphorylated state, have shown that the binding of JM to KD results in the inhibition of kinase activity of several RTKs (PDGFR (*11*); Eph-family RTKs (*12*); MuSK (*13, 14*); Flt3 (*15*); FGFR1 (*16*); Kit (*16, 17*)). One example is the ephrin receptor B2 (EphB2) in which the JM-KD interaction down-regulates activity through stabilization of the inactive conformation and constraint of the A-loop (*12*). In contrast, the full activity of epidermal growth factor receptor (EGFR) requires the presence of JM which links the asymmetric dimer via a 'latch' sequence (*18, 19*). The impact of CT on KD regulation has also been shown to be important in several RTKs. For instance, CT inhibits access of substrates to KD in the unphosphorylated Tie2 receptor (*20*). CT also suppresses the catalytic activity of EGFR through stabilization of an unphosphorylated inactive symmetric dimer (*9, 21–24*). The importance of CT in controlling pathogenic signal transduction is demonstrated in the expression of the constitutively active, oncogenic FGFR2 K-*sam*II gene (*25*). There are three variants of K-*sam*II which produce different length truncations of CT (Fig. 1A). Cells in which the truncated K-*sam* gene is amplified exhibit a growth advantage in gastric cancers. Expression of a C3 severely truncated variant in T24 bladder cells leads to un-regulated proliferation (*26*). Thus, the presence of CT prevents proliferative signaling from FGFR2 through an imprecisely known mechanism.

Our current knowledge of the regulatory roles of JM and CT is restricted to experiments based on the unphosphorylated KD with either JM or CT independently. The potential for cooperation between JM and CT towards regulation of the mono-phosphorylated, active intermediate state of the KD in the absence of RTK stimulation remains unexplored. FGFR2 provides a good example of a highly regulated RTK, particularly since the A-loop Y657-mono-phosphorylated state prevails under unliganded conditions (*4*). In this state FGFR2 is primed to respond rapidly to growth factor binding to produce the phosphorylated platform for recruitment of downstream effector proteins, but is subjected to stringent controls. Here we reveal the intricate mechanism by which the interplay of JM and proline-rich sequences on CT enable the receptor to sustain the active intermediate under non-stimulated conditions, and yet inhibit further catalytic activity. Our data also provide a rationale for the uncontrolled proliferation of the K-*sam* C-terminally truncated variants. Since virtually all RTKs possess JM and proline-rich sequences within their CT regions, this fine-tuning of regulation by JM and CT is likely to be conserved across RTKs. Indeed,

90   mutations of proline residues on numerous RTK CTs are connected to dysregulation of kinase activity

91   (*27–29*) leading to a range of human pathologies.

Results

Activity of KD is enhanced in the presence of JM

JM of FGFR family receptors was predicted to play an autoinhibitory role on KD activation (*16*), however, direct evidence of this is lacking. The impact of JM (residues 414-465) on kinase function was investigated through four dephosphorylated FGFR2 JM-KD constructs with progressively increasing truncations of JM. The rate of phosphorylation of KD was greater with intact JM (Fig. 1B). However, deletion of the entire JM resulted in phosphorylated product, as would be expected for an unencumbered enzyme in solution. The influence of JM on phosphorylation was measured in HEK293T cells over-expressing full length FGFR2IIIb (KGFR/K-*sam*-IIC1, C1 isoform, FGFR2^{C1}) including short, intermittent JM fragment deletions (Fig. 1C). Immunoblotting the A-loop phosphorylated tyrosines (pY657/pY658) in both basal and FGF7-stimulated phosphorylation of FGFR2^{C1} was significantly reduced in all JM deletion variants confirming the importance of the intact JM.

To understand the precise regulatory function associated with JM to KD interaction in FGFR2, we sought to understand the effect of progressive phosphorylation of KD on JM binding. Direct interaction between an MBP-JM and a series of six mutants that mimic the sequential phosphorylation pattern of KD (KD^{pY1} to KD^{pY6}; schematic Fig. 1D and fig. S1A) revealed that JM bound most strongly to the mono-phosphorylated KD^{pY1} (i.e. the 'active intermediate' state. Fig. 1d. $K_{d,app}$ = 2.51 ± 0.20 µM; Table S1 and Fig. 1E and fig. S1B). The affinity of JM for KD reduced with progressive phosphorylation. Only weak binding was apparent with the unphosphorylated, catalytically inactive K518I mutant, KD^{K518I}.

To determine the precise region through which JM and KD interact, we generated five JM peptides of 15-16 amino acids and measured their affinities to KD^{pY1} (table S1 and fig. S1C). ^{414}PAVHKLTKRIPLRRQVT^{430} demonstrated the tightest binding (K_d = 36.8 ± 6.2 µM) while ^{407}KPDFSSQPAVHKLT^{420} bound only three-fold weaker. These peptides share the consensus sequence ^{414}PAVHKLT^{420} proximal to the N-terminal of JM.

KD residues that interact with JM were identified by NMR. Titration of JM into ^{15}N-labelled KD^{pY1} led to major chemical shift perturbations (CSPs) in the N-lobe of KD^{pY1} resulting from changes in chemical environment on binding; including residues 464-472 (Fig. 1F) as well as 486 and 495 (Fig. 1G) (see fig. S1D for the assignment coverage and fig. S1E for HSQC titration spectrum). Notable CSPs were also observed in residues located within the αC helix (525-530; fig. S1F), which is a dynamic regulatory element of the KD. This suggests a mechanism whereby the binding of JM to the intermediate KD^{pY1} state would promote further kinase activity.

JM binding enhances asymmetric KD dimer formation

Asymmetric dimerization is crucial for receptor enzymatic function. Having shown that binding of JM is important in promoting kinase activity, we next investigated the impact of JM on dimerization. A series of JM-KD polypeptides exhibiting progressively increasing phosphorylation states (fig. S2A and S2B) exhibited the highest dimer population in the mono-phosphorylated state, JM-KD^{pY1} (Fig. 2A). In both the catalytically inactive mutants JM-KD^{K518I} and JM-KD$^{Y657/658F}$, dimerization was abrogated. The dependence of both JM binding and dimerization on the phosphorylation state of KD is consistent with JM acting as an intermolecular latch which is released with increasing pY burden.

To establish further how the JM affects the dimeric state of KD^{pY1} we used three JM-KD^{pY1} constructs with progressively truncated JM (schematic Fig. 2B). Truncation of JM resulted in an increase in the population of dimers, with isolated KD^{pY1} showing the greatest population of dimer. We quantified the 'apparent' dimerization constant of the mono-phosphorylated KD in the absence of JM (KD^{pY1}: $K_{d,app}$ =

135   112 ± 9 nM; fig. S2C). When JM was present the dimerization affinity was reduced by an order of
136   magnitude (JM-KD^{pY1}: $K_{d,app} = 3.46 \pm 0.10$ µM by MST (fig. S2C) and $K_{d,app} = 3.07$ µM by surface
137   plasmon resonance, SPR (fig. S2D)). This, somewhat counter-intuitive result, suggests that although the
138   presence of JM increases phosphorylation, it weakens dimerization of the KD. It also confirms that KD^{pY1}
139   and JM-KD^{pY1} dimers are conformationally different.

140   This was confirmed using small angle X-ray scattering (SAXS). In the absence of JM, KD^{pY1} scattering
141   consistently revealed equilibrium between monomers, symmetric head-to-tail dimers and additional larger
142   particles, possibly residual non-specific higher-order forms (fig. S2E and table S2). The symmetric dimer
143   corresponds to that depicted in crystal structures of inactive FGFR2 (PBD 2PSQ (30); KD05 in fig. S2E)
144   where access to the active site, and the positioning of the A-loop of one molecule are all encumbered by
145   the presence of the second molecule. In stark contrast to KD^{pY1}, in the selected ensembles of the extended
146   JM-KD^{pY1} the symmetric head-to-tail dimer was replaced by asymmetric dimers, with ~ 10% of these
147   loosely connected through JM (Fig. 2C). This dramatic redistribution of polypeptide conformations is
148   consistent with that required to produce the reduction in dimer affinity observed for JM-KD^{pY1} compared
149   to KD^{pY1} (fig. S2C). The structures of these dimers are reminiscent of reported structures of the
150   asymmetric conformations of enzyme-like (aka. receiver) and substrate-like (aka. activator) KDs caught
151   in the act of trans-phosphorylation (30, 31). In these modelled dimeric structures, JM from one protomer
152   binds to the other protomer, leaving one JM unoccupied (fig. S2F). Collectively, our data suggest that in
153   the absence of ligand stimulation, through forming a latch which stabilizes the asymmetric conformation
154   between mono-phosphorylated KDs, and hence abrogating symmetric dimer formation, JM is able to
155   sustain a dynamic relationship between mono-phosphorylated KDs from two FGFR2 molecules to
156   promote kinase activity and facilitate access to substrate sites. This then requires that additional control
157   mechanism(s) have to be in place to prevent unrestrained phosphorylation of the active intermediate.

158   Further detail of KD^{pY1} was provided by its 2.5 Å crystal structure determined in complex with a non-
159   hydrolysable ATP analogue (PDB ID 6V6Q, table S3). The asymmetric unit contained four molecules
160   which were arranged in two symmetric head-to-tail dimers (Fig. 2D and fig. S2G). These dimers
161   correspond to the symmetric dimers observed in SAXS (fig. S2E). Two of the four molecules in the
162   asymmetric unit showed well-defined electron density for the A-loop clearly featuring pY657 (fig. S2H).
163   pY657 is positioned within a single turn α-helix, and the phosphate is coordinated by three arginine
164   residues: R626, R650 and R665 (Fig. 2E). Burial of pY657 in this way has important consequences for
165   A-loop mobility and sustaining the mono-phosphorylated state. In support of our SAXS data, the dimeric
166   juxtaposition of KD^{pY1} is the same as that adopted in the published unphosphorylated kinase structure
167   (PDB 2PSQ; Fig. 2D and fig. S2G) even though 2PSQ crystals do not contain ATP and form a different
168   crystal lattice. The only notable differences between the two structures are found in the A- and nucleotide-
169   binding loops. In contrast to our structure, the A-loop tyrosine residues Y656 and Y657 (corresponding to
170   Y657 and Y658 in FGFR2IIIb) are solvent exposed in 2PSQ (Fig. 2E). KD^{pY1} also shows features similar
171   to the dually phosphorylated active substrate-bound kinase structure (PDB 2PVF; fig. S2I). The
172   orientation of N and C-lobes, the αC helices, and the catalytic residues K518 and E535 in the KD^{pY1}
173   structure are superimposable with 2PVF. However, the A-loop in 2PVF does not fold into a helix around
174   pY657, but instead is linear (Fig. 2F). We concluded that in the absence of JM, KD^{pY1} forms a symmetric
175   dimer which imposes constraint on the A-loop resulting in occlusion of access of substrate and corrupts
176   the site for correct placement of the γ-phosphate of ATP in the active site. The symmetric KD dimer
177   structure is potentially relevant to the unphosphorylated receptor or when KD is constrained as part of the
178   GRB2-bound heterotetramer (4). Furthermore, the engulfment of pY657 in the kinase core provides a
179   possible mechanism to preserve the active intermediate mono-phosphorylated state.

180 To determine whether JM from the enzyme-like, or substrate-like protomer forms the latch and
181 facilitates trans-phosphorylation, we incubated catalytically inactive KD^{K518I} (the substrate) with JM-
182 KD^{pY1} or KD^{pY1} (the enzymes). In this case the presence of JM increased phosphorylation of KD^{K518} (fig.
183 S2J). We then incubated KD^{pY1} (the enzyme) with JM-KD^{K518I} or KD^{K518I} (the substrates) and observed
184 no difference phosphorylation of the two substrates (fig. S2K). Deletion of $^{420}TKR^{423}$ and $^{426}RRQ^{428}$ on
185 the enzyme-like JM-KD^{pY1} (within the $^{414}PAVHKLTKRIPLRRQVT^{430}$ KD^{pY1}-binding sequence), had the
186 biggest impact on down-regulating phosphorylation of KD^{K518I} (fig. S2L). Our data show that in the active
187 intermediate state JM from the enzyme-like protomer latches on to the substrate-like protomer in the
188 asymmetric active dimer and increases the phosphorylation of the latter molecule. In the absence of other
189 regulatory interactions, this latch holds the active KDs such that they can interact with one another, whilst
190 being prevented from self-association into the inactive symmetric dimer.

Activity of KD is inhibited by CT

192 To investigate the detailed regulatory function of CT, we first measured the impact on receptor activity of
193 N-terminally Flag-tagged, FGFR2IIIb C-terminally truncated C1, C2, C3 K-*sam*II isoforms. HEK293T
194 cells transfected with $FGFR2^{C1}$; $FGFR2^{C2}$; $FGFR2^{C3}$ or $FGFR2^{C1\Delta34}$ ($FGFR2^{C1}$ with 34 amino acids
195 deleted from the C-terminus that is identical in length to C2 but does not contain the Q779P, S783C and
196 T787P mutations which produce a sequence of two consecutive PXXP motifs: CT sequences shown in
197 Fig. 3A) revealed that deletion of CT led to increased receptor phosphorylation and activation of effector
198 proteins under both unliganded and FGF7-stimulated conditions (Fig. 3A, $FGFR2^{C1\Delta34}$). The absence of
199 CT in $FGFR2^{C3}$ promoted downstream signalling in both ERK1/2 (MAPK) and AKT pathways without
200 ligand stimulation. This is likely to be due to the binding of the scaffold protein FRS2 which is known to
201 bind to the JM and mediate downstream effector protein recruitment to the activated receptor (Fig. 3A)
202 (*32*) (in contrast to FGFR1 to which FRS2 is constitutively bound; (*33*)). This result strongly suggests that
203 the presence of CT controls FGFR2 kinase activity as well as inhibiting the interaction of FRS2 with the
204 receptor.

205 We next investigated the direct effect of CT on the regulation of FGFR2 kinase activity using
206 recombinant protein. Consistent with the cell-based assay (Fig. 3A), the phosphorylation of the A-loop
207 increased as CT was truncated (KD-CT^{C3} Fig. 3B). Thus, KD-CT^{C3}, like KD^{pY1} which appeared in
208 dynamic equilibrium between monomers and symmetric head-to-tail dimers (Fig. 2B, 2D and fig. S2E),
209 behaved as a free enzyme (Fig. 1B). As expected, KD-CT^{C1} had the lowest kinase activity but CT in KD-
210 $CT^{C1\Delta34}$ released inhibition as seen in our cell-based assay. However, KD-CT^{C2}, which is of an identical
211 length, but includes similar PXXP motifs as present in KD-CT^{C1}, restored the inhibitory capability. This
212 result suggests the importance of the PXXP motif(s) of CT in the inhibition of kinase activity.

A proline-rich motif on CT is required for the binding to KD

214 So far, our data indicate that when CT is present it inhibits the active intermediate receptor from
215 progressing to the fully phosphorylated state. This was hypothesized to occur via two distinct mechanisms;
216 1) antagonistically blocking receptor activation through direct binding to KD, and/or 2) through binding
217 of CT to KD and/or JM to inhibit formation of asymmetric dimer.

218 CT^{C1} bound to KD^{pY1} with a moderate affinity ($K_d = 3.75 \pm 0.46$ µM; Fig. 3C). Although KD^{pY1} is
219 potentially in the form of a dimer, the profile of the binding curves suggests that CT binds independently
220 to the domain. NMR spectroscopy was used to probe the interaction surfaces of CT^{C1}. To this end, CSPs
221 of ^{15}N-labelled CT^{C1} were measured on addition of KD^{pY1} (Fig. 3D). Two distinct potential interacting
222 regions of CT^{C1} were observed; residues around 765 to 780, including the known binding site for
223 downstream effector proteins Y770 (Fig. 3D), and residues within the proline-rich motif in the C-terminus

224   (D802 to Y813: Fig. 3D). In a separate experiment CT^{C1} was divided into two fragments: the first 24
225   residues 765-788 ($CT^{C1\Delta34}$) and the last 23 residues 800-822 (CT^{L23}). $CT^{C1\Delta34}$ revealed negligible CSPs
226   changes (fig. S3A and S3B) which supported our previous kinase assay data which showed that in the
227   absence of the PXXP motifs this region does not affect kinase activity. More significant CSP changes
228   from CT^{L23} were observed (fig. S3C and S3D). We concluded that the last 23 residues containing the
229   PXXP motifs are necessary for binding with the KD^{pY1}, and this facilitates subsequent engagement of the
230   first 24 residues of CT^{C1}. CSP and affinity measurements of peptide fragments of CT revealed that the
231   tightest binding sequence was ^{801}PDPMPYEPCLPQYPH^{815} ($K_d = 25.9 \pm 5.4$ µM; table S1 and fig. S3E).
232   Our NMR experiments confirm that although a potentially extensive interface is involved, the PXXP
233   motifs are required for CT^{C1} to interact with the active intermediate KD^{pY1} and hence inhibit kinase
234   activity.

235   The importance of individual proline residues within the PXXP motif in binding to KD^{pY1} was
236   investigated using an *in vitro* GST pulldown assay with both the GST-tagged CT^{C1} and CT^{C2} (Fig. 3E).
237   Binding was significantly reduced in the presence of proline to alanine point mutations except for P801A
238   and P814A. The mutation of both P803 and D802 had a large impact on binding. Supported by our kinase
239   assay and NMR data, we found that GST-CT^{C2} bound to KD^{pY1} whilst the first 24 amino acids (GST-
240     $CT^{C1\Delta34}$) of C1 did not. The similarity of CT^{C2} with the wild type CT^{C1} was also apparent in the kinase
241   phosphorylation data (Fig. 3B). Sequence alignment suggests that the interactions are strongest when the
242   sequence includes a PXEPXXPXYP motif (where X is any residue) which occurs between residues 805
243   and 814 for CT^{C1} and 776 and 785 for CT^{C2}.

244   Point mutations in $FGFR2^{C1}$ PDPMPXEPXXPXYP sequence confirmed the importance of this region
245   for signaling in HEK293T cells (Fig. 3F). Even in the absence of FGF7 the corruption of the proline-rich
246   sequence had a dramatic affect in up-regulation of FGFR2 and its downstream ERK1/2 signalling.
247   Inhibition of recombinant KD by incubating peptides derived from CT^{L23} identified ^{808}PCLPQYPH^{815} as
248   the minimum sequence of CT required for KD down-regulation (Fig. 3G and table S1 for sequences).

The CT-KD interface includes regions associated with kinase activity

250   Having established a detailed knowledge of the residues from CT that interact with KD^{pY1}, we also
251   measured CSP data for ^{15}N-labelled KD^{pY1} on addition of CT. (Fig. 4A). Mapping the perturbed residues
252   onto the crystal structure (Fig. 4B) revealed four clusters of residues in the KD^{pY1} that showed significant
253   shifts: 470-490 at the very N-terminal end of the N-lobe (including the nucleotide binding loop); 515-525
254   (including the regulatory αC helix); 590-610 (including the kinase insert), and 710-740 at the very C-
255   terminal end of the C-lobe. The interface between CT^{C1} and KD^{pY1} is therefore extensive and covers
256   regions associated with kinase activity providing a rationale for the inhibitory nature of the direct
257   interaction. Comparing CSPs for binding of JM to KD^{pY1} (Fig. 1F) and CT to KD^{pY1} (Fig. 4A) suggests
258   that there is some overlap, although residues with the largest CSPs are not entirely coincident. We
259   performed HSQC titration of JM with ^{15}N-labelled KD^{pY1} and recorded the CSPs for residues in regions
260   previously seen to interact with JM on KD^{pY1} (464V, 466E, and 467F at the N-terminal lobe and 530S and
261   532L on the αC helix: fig. S4A, left panels). Subsequent titration of CT to the preformed JM-KD complex
262   resulted in negligible CSP effects on the JM-bound KD^{pY1} spectra (fig. S4A, right panels) underscoring
263   that binding of CT does not compete directly with JM for binding to KD^{pY1}.

CT inhibits asymmetric dimerization of JM-KD^{pY1}

265   When JM is present with KD^{pY1} an asymmetric dimer forms which can promote further kinase activity.
266   Conversely the presence of CT with KD inhibits this activity. We therefore sought to understand how
267   these opposing control mechanisms combine to regulate further activity of KD^{pY1}. Using size exclusion

268 chromatography, we showed that CT was able to block dimer formation when included as part of KD^{pY1}-
269 CT (Fig. 5A). GST-CT^{C1} was able to pull down (Fig. 5B) and form a high affinity complex with JM-
270 KD^{pY1} (SPR, K_d = 165.2 ± 1.6 nM; MST, K_d = 304 ± 44 nM: table S1, Fig. 3C and fig. S5B respectively).
271 The binding of CT to JM-KD^{pY1} was able to disrupt the asymmetric dimerization of the construct, as
272 demonstrated using steady-state fluorescence resonance energy transfer (FRET) measurement (fig. S5A).
273 Increasing the phosphorylation state of KD reduced the affinity of CT (fig. S5B). CT can bind to the non-
274 phosphorylated JM-$KD^{Y657/658F}$ but with reduced affinity (K_d = 5.65 ± 1.9 μM; table S1). It is notable that
275 since the binding of CT to JM-KD^{pY1} disrupts the asymmetric dimerization of the latter, the resulting high
276 affinity complex has molecular ratio CT:JM-KD^{pY1} of 1:1.

277 To confirm the impact of the CT on dimer formation in cells we used fluorescence lifetime imaging
278 microscopy (FLIM) in serum starved HEK293T cells co-expressing CFP- and RFP-tagged $FGFR2^{C1}$,
279 $FGFR2^{C2}$ and $FGFR2^{C3}$. Compared to the control ($FGFR2^{C1}$ with RFP) we saw increasingly shorter
280 lifetimes in the populations of C2 and C3 receptors respectively, indicating that, in the absence of growth
281 factor, dimerization increases in response to reduction in the size of CT (Fig. 5C). Interestingly the C3
282 isoform appears to be extensively membrane localized suggesting that recycling of the receptor was
283 impaired (zoomed inset panels Fig. 5C). Together our data indicate that the binding of CT to active
284 intermediate KD^{pY1} counters the positive impact of JM on RTK phosphorylation in the absence of stimuli
285 by simultaneously binding to regions of KD inhibiting enzyme activity as well as restricting formation of
286 the asymmetric dimer, i.e. involving both mechanisms hypothesised earlier.

CT binds independently to JM

288 We have shown that CT binds more tightly in a 1:1 complex to JM-KD^{pY1} than to KD^{pY1} alone (Fig. 3C).
289 We have also demonstrated that, although JM acts to sustain the asymmetric dimer and hence enhance
290 activity, only the N-terminal residues of JM are involved in the intermolecular latch interaction. Thus, CT
291 might be capable of binding to both KD^{pY1} and JM. To investigate a direct intramolecular interaction
292 between JM and CT we first showed that binding of JM-KD^{pY1} to both CT^{C1} and CT^{C2} was reduced as JM
293 was truncated (Fig. 5D and 5E respectively). Since stoichiometry of the final complex formed in each case
294 is 1:1, the self-associated state of the JM-KD^{pY1} interactant should not produce the observed changes in
295 binding. Interaction with CT was much reduced on deletion of residues 429 to 449 which are outside the
296 region previously shown to bind to KD. Thus, it would be possible under certain conditions (e.g. within
297 the context of the ligand bound full length receptor) that JM could maintain the latch interaction whilst
298 simultaneously binding to CT. This suggests that CT has two independent modes of binding involved in
299 RTK regulation: 1) binding to KD^{pY1} and inhibiting activity and dimerization, and 2) binding to JM
300 without affecting latch formation. These modes will have distinct function, are mutually exclusive and
301 occur at different time points in receptor up-regulation.

302 Using four mono-phosphorylated constructs; KD^{pY1}, JM-KD^{pY1}, KD^{pY1}-CT^{C1}, and JM-KD^{pY1}-CT^{C1} in
303 a pull-down assay with GST-CT^{C1}, we showed that CT^{C1} binds independently to JM-KD^{pY1}. However,
304 when CT was included as part of the construct in both KD^{pY1}-CT^{C1} and JM-KD^{pY1}-CT^{C1} binding was
305 abrogated (Fig. 5F). Thus, our data demonstrate that CT binds to JM-KD^{pY1} through an intramolecular
306 interaction, since including CT on the construct disrupts dimerization and blocks GST-CT binding. We
307 know that CT forms an extensive intramolecular interface with KD^{pY1} which stabilizes the monomeric
308 protomer. This interface includes residues across the extent of the entire tail region (Fig. 3D). We have
309 also shown that the presence of JM enhances the interaction with CT. Incubation of the same KD^{pY1}, JM-
310 KD^{pY1}, KD^{pY1}-CT^{C1}, and JM-KD^{pY1}-CT^{C1} with GST-JM showed that, consistent with previous
311 observations, JM was able to bind to KD^{pY1} (Fig. 5G). JM also bound JM-$KD^{pY1,}$ which, although
312 dimerized through one JM latch, has a free KD for independent JM binding. Significant binding of JM to

313 KD^{pY1}-CT, but negligible binding of JM with the JM-KD^{pY1}-CT^{C1} construct was observed. These
314 interactions of JM in the presence of CT could not occur if CT successfully competed with JM for binding
315 to KD, but would require that JM can bind simultaneously with KD and CT. We measured direct binding
316 between JM and CT (K_d = 20.2 ± 2.92 μM; table S1 and Fig. 5H). We also identified that the highest
317 affinity sequence of JM that recognized CT includes residues ^{429}VTVSAESSSSMNSN^{442} (fig. S6A and
318 table S1). Thus, the binding site on JM for CT is non-overlapping and C-terminal to the consensus
319 sequence of JM that we showed is required for forming the intermolecular latch to KD^{pY1}, i.e.
320 ^{414}PAVHKLT^{420}, however it includes the VT site (including residues V429 and T430; the VT motif) (*34*)
321 for FRS2 recruitment on growth factor binding. These data rationalize our previous cell-based observation
322 that the presence of CT prevents FRS2 phosphorylation by FGFR2 under stimulated conditions (Fig. 3A).

323 To map the interaction between JM onto CT^{C1} we titrated unlabelled JM into ^{15}N-labelled CT^{C1}. The
324 binding site can be seen to incorporate residues between V798 and S819 of CT which contains the proline-
325 rich motif (Fig. 5I). Using a series of short peptides derived from CT we demonstrated that the proline-
326 rich sequence from CT binds to JM (table S1 and fig. 6b), and the ^{808}PCLPQYPH^{815} sequence is necessary
327 for CT to bind to JM. Importantly, this is the same sequence that binds to both KD (Fig. 3) and to the
328 GRB2 CSH3 domain (*35*). Thus, CT mediates three modes of receptor regulation.

329 The ability of CT to bind mutually exclusively to both KD and JM suggests that it can adopt two distinct
330 conformations which have opposing impact on kinase activity, and which operate independently at
331 different time points in the receptor up-regulation process. 1) Binding of CT to KD^{pY1} results in an
332 intramolecular auto-inhibitory conformation which sustains the monomeric state of the mono-
333 phosphorylated receptor. This is expected to control the active intermediate state in the absence of growth
334 factor stimulation. 2) The CT of the enzyme-like KD flips from the inhibitory interaction with KD^{pY1}, to
335 bind intramolecularly to the JM. In this state JM can simultaneously perform the role as the latch to the
336 substrate-like KD of the asymmetric dimer. Thus, the CT is effectively isolated from blocking the kinase
337 activity and receptor dissociation. Also in this state the CT of the substrate-like protomer is free to become
338 phosphorylated. We propose that CT is stabilized in the latter of these two conformations when the
339 receptor is bound to extracellular growth factor. The direct interaction between two peripheral regions
340 thus adds a level of control to the kinase output not previously observed for RTKs.

341 **KD can exist in equilibrium between Grb2-bound and CT-bound active intermediate states**

342 Previously we have shown that in the absence of growth factor FGFR2 binds to the C-terminal SH3
343 domain of dimeric GRB2 through the proline-rich sequence on CT (^{808}PCLPQYP^{814}) and maintains
344 FGFR2 in an active intermediate, signalling incompetent heterotetrameric state (*4, 36*). Since we have
345 shown that the proline-rich sequence binds intramolecularly to JM-KD^{pY1}, the ability of CT to regulate the
346 active intermediate state is manifold. To assess whether these interactions are mutually exclusive, we first
347 performed a pulldown assay using GST-CT which was incubated with GRB2. Subsequent addition of
348 increasing concentrations of JM-KD^{pY1} gradually decreased the amount of GRB2 precipitated, suggesting
349 JM-KD^{pY1} competes with GRB2 for the binding site on CT (fig. S6C). Based on the respective measured
350 affinities, it is assumed that CT was binding to KD rather than JM in this experiment. CT was then
351 immobilized on biolayer interferometry (BLI) sensors to probe the competitive interactions of JM-KD^{pY1}
352 and GRB2. Binding of JM-KD^{pY1} or GRB2 alone to the immobilized CT showed the expected different
353 interaction properties associated with the size of the added proteins (fig. S6D) however, the addition of
354 both JM-KD^{pY1} and GRB2 simultaneously gives an identical response to that of adding only JM-KD^{pY1}
355 to immobilized CT (fig. S6D), suggesting that GRB2 competes less efficiently with JM-KD^{pY1}. Sequential
356 binding of JM-KD^{pY1} and GRB2 to the immobilized CT (fig. S6E) also indicated that, once CT is saturated
357 with JM-KD^{pY1}, GRB2 cannot compete it off. Interestingly, application of JM-KD^{pY1} to GRB2-saturated

358 CT sensor resulted in a decrease of the binding signal followed by an increase of interaction signal as the
359 JM-KD^{pY1} displaces GRB2 on the immobilized CT (fig. S6F). Thus, equilibrium between CT bound to
360 GRB2 and CT bound to JM-KD^{pY1} exists but the respective affinities and the intramolecular nature of
361 interaction strongly favours the latter.

JM and CT regions combine to regulate kinase activity

363 Having demonstrated the positive and negative impacts of JM and CT binding on regulation of KD^{pY1}
364 respectively, we examined how the presence of these peripheral regions control FGFR2 signalling. The
365 following constructs, KD^{pY1}; JM-KD^{pY1}; KD^{pY1}-CT^{C1}; and JM-KD^{pY1}-CT^{C1} were used in an assay with
366 the kinase dead JM-KD^{K518I}-CT as a substrate (Fig. 6A). The activity is slightly enhanced by the presence
367 of JM in JM-KD^{pY1} compared to KD^{pY1}. This is consistent with JM stabilizing the active asymmetric
368 dimer. Conversely, the presence of CT in KD^{pY1}-CT^{C1} dramatically inhibits kinase activity through
369 previously observed direct interaction with KD and resulting inhibition of dimerization. The presence of
370 JM and CT in JM-KD^{pY1}-CT^{C1}shows medium activity. This underscores the regulatory role of the
371 interplay between the two peripheral regions of the receptor in sustaining the active intermediate state
372 through modulation of kinase activity. These data mirror the experiments on the constitutively active
373 truncated K-*sam* FGFR2 isoforms, where the absence of CT leads to dysregulation of the intact receptor
374 (Fig. 3A).

375 As the receptor becomes progressively phosphorylated the interaction of CT to KD needs to be down-
376 regulated to enable access of downstream signalling proteins. We used a pull down experiment to reveal
377 the mechanism for this release. GST-CT which was phosphorylated on its available tyrosine residues,
378 pCT^{C1}, was unable to pulldown JM-KD as it became progressively phosphorylated, i.e. JM-KD^{pY1} to JM-
379 KD^{pY6} (Fig. 6B) Thus, as the receptor pY load increases, the phosphorylated CT is less able to bind
380 intramolecularly, making it available for recruitment of downstream effector proteins.

381 We have shown that residues in JM sequence 429 to 449 play a role in interacting with CT (Fig. 5D),
382 and hence the presence of CT would occlude the ^{429}VT^{430} binding motif (*34*) for the FRS2 phosphotyrosine
383 binding domain (PTB) in the absence of stimulation and prevent aberrant signalling. Therefore, the
384 absence of CT in the C3 isoform should allow unrestricted recruitment of FRS2 leading to prolonged
385 phosphorylation even at the unliganded state (as seen in Fig. 3A). This inhibition of access of FRS2 to JM
386 by CT was demonstrated where significantly less JM-KD^{pY1}-CT^{C1} was precipitated compared to JM-
387 KD^{pY1}-CT^{C3} in a pull down assay using GST-FRS2 PTB domain (Fig. 6C). JM-KD^{pY1}-CT^{C2} showed an
388 intermediate level of interaction consistent with the proline-rich motif present in this isoform binds with
389 lower affinity to the FRS2 cognate site. We also measured different FGFR2 isomers binding to FRS2
390 using BLI. In the absence of the intact CT (C3 isoform) a significantly increased amount of FGFR2 protein
391 bound to the PTB domain compared with the C1 and C2 isoforms (Fig. 6D).

392 Using an *in vitro* kinase assay we were able to demonstrate that the phosphorylation of FRS2 by FGFR2
393 is affected by CT in the different isoforms. Immunoblotting showed that the C3 isoform has the highest
394 kinase activity toward FRS2, whereas the C1 isoform has the lowest (Fig. 6E). This further suggested that
395 CT^{C1} isoform can interact with JM which contains the ^{429}VT^{430} motif, and inhibit the recruitment and
396 phosphorylation of FRS2 in the active intermediate state. This observation explains why the C3 isoform
397 has higher FRS2-mediated downstream signalling activity and exhibits uncontrolled activation leading to
398 oncogenic outcome in the active intermediate state.

General importance of proline-rich motifs in RTK regulation

400 Having shown that proline-rich motifs are critical in regulatory interactions with JM and KD, and the
401 mutations on proline residues affect FGFR2 kinase activity and downstream signalling, we investigated
402 whether mutation/truncation of proline-rich motifs within CTs of other RTKs are found in cancers in
403 general. Humans have 58 identified RTKs, which fall into twenty subfamilies (*10*) of which 49 have
404 proline residues on their CTs. Apart from providing protein recruitment sites for SH3/WW domains, the
405 importance of proline-rich motifs in RTK signalling has not been investigated. Genomic data from cancer
406 patient samples available on cBioPortal for Cancer Genomics (www.cbioportal.org) shows that of the 49
407 RTKs, 40 have been identified with proline residue point mutations or deletions of proline-containing CT
408 sequences (table S4). This suggests an important role for proline-containing sequences and raises their
409 importance in regulation, particularly during the non-stimulated, active intermediate state we present here.

410 **Discussion**

411 RTKs generally cycle through a series of states on going from the dephosphorylated monomeric state to
412 the fully phosphorylated, signalling-competent state. We have investigated a series of snapshots of
413 structural states which show possible interactions and juxtapositioning of the various components. Linking
414 of these snapshots into an animated series permits a full understanding of the progression of events and
415 how each one provokes the next. Our data have highlighted RTKs in the mono-phosphorylated active
416 intermediate JM-KD^{pY1}-CT state as the most important frame in the animation of the progress from
417 inactive to signalling receptor. This state represents a major check-point because the KD is active, but
418 signal transduction is inhibited. Our observations show how, in this state, the receptor is highly regulated
419 by the interactions of JM and the proline-rich motif on CT in the absence of stimulation, whilst being
420 primed for full activation on growth factor binding.

421 Our mechanistic model starts with the dephosphorylated, inactive monomeric state, and progresses via
422 the mono-phosphorylated active intermediate, through to the fully active state (Fig. 6F). Under basal
423 conditions growth factor receptors diffuse through the plasma membrane (Fig. 6F i). Random collision
424 leads to transmembrane-mediated self-association. This can lead to as much as 20% dimer and subsequent
425 A-loop tyrosine phosphorylation of FGFR2 in the absence of ligand (*3*). Binding of GRB2 stabilizes
426 FGFR2 dimers in the active intermediate state and inhibits further phosphorylation (*4*) (Fig. 6F ii). The
427 presence of GRB2 on CT of FGFR2 is perturbed by a cycle of phosphorylation by the receptor and
428 subsequent dephosphorylation by SHP2 phosphatase (*4, 36*). Without the inhibitory function of GRB2,
429 the dysregulated active intermediate receptor could progress to full activation through the formation of
430 asymmetric dimer mediated by JM. This would leave receptor activation in a precarious position without
431 an additional mechanism restrict further kinase activity. Our observations demonstrate that this
432 mechanism involves the intramolecular binding of CT to JM-KD^{pY1} (Fig. 3C). This interaction is mutually
433 exclusive of binding of GRB2 (fig. S6C to S6F and Fig. 6F iii). The presence of CT inhibits further
434 phosphorylation by inhibiting catalytic activity and asymmetric dimerization. Thus, the mono-
435 phosphorylated state, which is the check-point prior to full receptor activation, is tightly regulated either
436 by the binding of GRB2 or the interaction with CT.

437 When cells are exposed to extracellular stimulation, JM of one protomer in the dimer latches onto KD
438 of the other (Fig. 6f iv). In this way the former becomes the designated enzyme-like receptor, whilst the
439 latter becomes the substrate-like receptor, both being held in a moderate affinity, dimeric conformation.
440 Since the KD is already in its mono-phosphorylated state it is available for JM binding and adoption of
441 the asymmetric dimer conformation. JM appears to inhibit the direct interaction between KDs and promote
442 dynamic interlocution between the active domains in an asymmetric dimer (Fig. 2C). It also juxtaposes
443 KDs within the asymmetric dimer to prevent progressive oligomerization of the domains (i.e. 'daisy chain'
444 formation (*18, 37*)) allowing only dimers to form.

The unrestricted activity of the enzyme-like receptor requires that CT is not able to bind to, and hence down-regulate KD of this protomer. This state is achieved through the intramolecular binding of CT to the available site on JM. Thus, the role of CT is multi-faceted and functions through independent interactions with GRB2, KD and JM. Truncation of CT up-regulates the kinase (Fig. 3A and 3B) and hence provides a rationale for the elevated proliferative signalling as we seen in the oncogenic K*sam* deletions (fig. S6G).

The release of negative control by CT promotes an increase in KD phosphorylation which weakens dimerization (Fig. 2A), enhancing the dynamic interplay between protomers permitting easier access to tyrosine sites and alternation of the enzyme-like and substrate-like states between the molecules. Increasing phosphorylation of KD also results in progressive weakening of interactions with the peripheral regions ultimately leading to kinase dimer dissociation, leaving the receptor in a highly phosphorylated state whereby it can recruit downstream effector proteins (Fig. 6F v). Dissociation of phosphorylated FGFR2 also leaves it exposed to phosphatase activity which ultimately returns it to its initial unphosphorylated state (Fig. 6F i). Clearly the controlled activation cycle of FGFR2 would be affected by the impact of additional factors such as endocytosis (*33*), fluctuations in GRB2 concentration (*38*) and phosphatase concentration (*36*). However, the importance of both peripheral regions in influencing the self-association, and the dimeric conformation underscores how the receptor is tightly regulated to avoid aberrant signalling during the progression from unphosphorylated inactive form to fully phosphorylated active form.

Different RTKs include features that enable idiosyncratic regulation and commitment to defined downstream outcomes. The presence of peripheral regions on the majority of RTKs suggests that these can play common roles. In particular, the prevalence of proline-containing sequences in CTs. The impact on kinase-driven pathology of their mutation/truncation highlights the regulatory importance of these sequences. Mutations within, or deletions of proline-rich sequences in CTs of many RTKs (including IGF1R, FGFR2, ERBB2, ERBB3, ERBB4 and ROR2) are associated with range of cancers (*27–29*) (table S4). We hypothesise therefore that, since these sequences are found in the majority of RTKs, their interaction with KD and/or JM is a common feature of RTK regulation. Our data show, in the case of the K-*sam*II truncations, that when these regulatory features are perturbed pathogenicity can result in uncontrolled cellular signalling. Thus, understanding of the roles of the peripheral region interactions will suggest alternative routes for therapeutic intervention outside the currently well-trodden path of inhibition of kinase activity.

Materials and Methods

Cell culture

HEK293T cells were maintained in DMEM (Dulbecco's modified Eagle's high glucose medium) supplemented with 10% (v/v) FBS (foetal bovine serum) and 1% antibiotic/antimycotic (Lonza) in a humidified incubator with 10% CO_2.

Protein expression and purification

All MBP-tagged, GST-tagged and 6xHistidine-tagged fusion proteins were expressed and purified from BL21(DE3) cells. A single colony was used to inoculate 100 mL of LB which was grown overnight at 37°C. 1L of LB was inoculated with 10 mL of the overnight culture and allowed to grow at 37°C until the OD_{600} reaches 0.8 at which point the culture was cooled down to 20°C. Expression was then induced with 0.5 mM IPTG and the culture was grown for a further 12 hours before harvesting by centrifugation. Cells were re-suspended in 20 mM Tris, 150 mM NaCl, 10% glycerol, pH 8.0 in the presence of protease

488 inhibitors and lysed by sonication. Insoluble material was removed by centrifugation (40,000g at 4°C for
489 60 min). The soluble fraction was applied to an appropriate affinity column (Amylose column for MBP-
490 tagged proteins, GST column for GST-tagged proteins and Talon column for His-tagged proteins).
491 Following a wash with 10 times column volume of wash buffer (20 mM Tris, 150 mM NaCl, pH 8.0), the
492 protein was eluted from the column with elution buffer (the washing buffer supplemented with 20mM
493 maltose for the MBP-tagged proteins; a supplement of 20mM reduced glutathione for the GST-tagged
494 proteins; a supplement of 150mM imidazole for the 6xHis-tagged proteins) and was concentrated to 5 mL
495 and applied to a Superdex 75 gel filtration column equilibrated in a buffer containing 20 mM HEPES, 150
496 mM NaCl and 1 mM TCEP pH 7.5. Analysis for protein purities by SDS-PAGE showed greater than 98%
497 purity. For CT (CT^{C1} and CT$^{C1\Delta34}$, GST-tagged) production and JM-KD^{pY1}-CT^{C1} (for crystallography,
498 6xHis-tagged), 1 unit of thrombin (Sigma T6884) was used to cleave 1mg of recombinant proteins at 4°C
499 for overnight. After cleavage, Benzamidine Sepharose 4 Fast Flow beads (GE) were used to remove
500 thrombin. GST-Tag/His-Tag and uncut proteins were removed by passing protein solution through a GST
501 or Talon column. Expression of ^{15}N-labelled proteins for NMR titrations and ^{2}H, ^{15}N, ^{13}C-labelled protein
502 for backbone resonance assignment was done as previously described(*39*). For expression in 100% D$_2$O,
503 this procedure was modified by pre-growing the culture in a small volume of 100% D$_2$O prior to
504 expression over 20 hours.

Nuclear magnetic resonance (NMR) spectroscopy

506 *General information*

507 All NMR spectroscopic experiments concerning KD backbone assignment were carried out on Bruker
508 Avance III 950 MHz NMR spectrometers equipped with cryogenically cooled triple resonance probes
509 (5mm TXO or 3mm TCI). Titration experiments were additionally carried on Bruker Avance III 750 MHz
510 NMR spectrometer, equipped with ^{1}H-optimized triple resonance NMR 5mm TCI-cryoprobe. NMR data
511 was processed using NMRPipe and further analyzed with CcpNmr Analysis software package available
512 locally and on NMRBox platform. Chemical shift perturbations (CSPs) were calculated from the chemical
513 shifts of backbone amide ^{1}H ($\Delta\omega_H$) and ^{15}N ($\Delta\omega_N$) using the following equation: CSP =
514 $\sqrt{\Delta\omega_H^2 + (0.154\Delta\omega_N^2)}$.

515 *KD and CT backbone assignment*

516 In order to obtain backbone assignment of KD and CT, both proteins were expressed in isotopically
517 labeled media as described above. Set of KD samples uniformly ^{13}C-^{15}N labeled and fully or partially
518 (70%) deuteriated (^{2}H) as well as uniformly ^{13}C-^{15}N-labeled CT were prepared. Spectra were recorded at
519 25°C with KD concentrations ranging from 200 µM to 600 µM in a HEPES buffer (20 mM HEPES, 150
520 mM NaCl and 1 mM TCEP pH 7.5). Spectra of CT were recorded using 300 µM sample in the same
521 HEPES buffer. Standard Bruker library together with BEST versions of amide transverse relaxation
522 optimized spectroscopy (TROSY) of 3D backbone resonance assignment pulse sequences (HNCA,
523 HNCOCA, HNCACB, CACBCONH, HNCO and HNCACO) were applied to collect high resolution
524 spectra. In order to shorten acquisition time, Non-Uniform Sampling (20-30%) was routinely used.

525 *KD titration with CT and CT-derived fragments*

526 The NMR titration of uniformly ^{15}N-labeled KD with unlabelled CT and CT-derived peptides were
527 recorded at 25°C using 100 µM KD sample in HEPES buffer. CT and CT-derived fragments were added
528 at the 1:0.5, 1:1, 1:1.5, 1:2 and 1:1, 1:5, 1:10 molar ratios respectively and the amide spectra were recorded
529 using BEST TROSY pulse sequence.

530 *CT titration with preform KD-JM complex*

531 The NMR titration of KD with JM peptide were recorded at 25°C using 250 μM uniformly ^{15}N-labeled
532 sample in HEPES buffer. JM peptide was added at the 1:1, 1:2 and 1:3 molar ratios and the amide spectra
533 recorded using BEST TROSY pulse sequence. To the fully titrated KD, peptide JM was added and the
534 amide spectra (BEST TROSY) recorded at 1:1, 1:2, 1:3 molar ratios.

CT titration with KD

536 The ^{15}N-labeled CT sample concentrated to 300 μM in HEPES buffer was titrated with unlabelled KD.
537 Amide spectra were recorded at 25°C using hsqcetfpf3gpsi pulse sequence from Brüker library at 2:1, 1:1,
538 1:2, 1:3, 1:4, 1:8 and 1:12 molar ratios.

X-ray crystallography

540 Crystals of JM-KD^{pY1}-CT^{C1} were obtained using the hanging-drop vapour diffusion method, mixing equal
541 volumes of protein with reservoir solution and equilibrating over this reservoir at 20°C for 2 weeks. The
542 reservoir solution contained 100 mM Tris, 160 mM TMAO, 20% PEG2000 at pH 8.6. For cryoprotection,
543 crystals were transferred in the crystallization buffer supplemented by 20% Glycerol. X-ray diffraction
544 data sets were collected from frozen single crystals at the Advanced Light Source (Berkley, CA, USA,
545 beamline 8.3.1) and processed with the program Elves. A molecular replacement solution was obtained
546 using the BALBES molecular replacement pipeline and the crystal structure PDB code 2PSQ. Iterative
547 model rebuilding and refinement was performed by using the program COOT, REFMAC5 and
548 PDB_REDO against the data set. Structural figures were made using PyMol.

Small-Angle X-ray Scattering (SAXS)

550 Data were collected for the mono-phosphorylated forms of KD^{pY1} and JM-KD^{pY1} on the SIBYLS beamline
551 at the Advanced Light Source, Berkeley, USA at a wavelength of 1 Å. Every sample was exposed
552 successively for 0.5, 1.0, and 6.0 s. Protein sample concentrations ranged from 1.0–10 mg/mL. Data for
553 protein sample and buffer alone and were recorded at 10°C, and the buffer contribution was subtracted
554 from the protein scattering data. Additional exploratory SAXS data were recorded at the SWING beamline
555 (SOLEIL, Saint-Aubin, France) at λ = 1.03 Å. Data were analysed using PRIMUS, GASBOR, DAMMIF,
556 and DAMAVER from the ATSAS software package 1. Model SAXS patterns were calculated and fitted
557 to data using FoXS 2. MultiFOXS was used to evaluate mixtures of monomers and dimers.

558 Swiss-Model was used to prepare a complete FGFR2 KD^{pY1} monomer (including loops and side chains
559 missing in the crystallographic model) based on PDB 2PVF. Potential FGFR2 KD^{pY1} dimers were based
560 on arranging the completed monomer into dimer configurations found in crystal structures: PDB 2PSQ
561 (symmetric head-tail dimer); 2PVF and 3CLY (asymmetric kinase C-terminal tail trans-phosphorylation);
562 3GQI (asymmetric A-loop trans-phosphorylation of FGFR1). Additional dimers were derived from our
563 FGFR2 KD^{pY1} crystal structures (PDB 6V6Q). These crystals were formed by a combination of the
564 symmetric head-tail dimers found in 2PSQ, as well as two other forms. In one, termed KI, contacts were
565 established through the kinase insertion (KI) loop. In the other, termed N-C, the N-lobe of one kinase
566 bound to the C-lobe of the other (See Supplementary Fig. 2d). 30 additional dimers were obtained using
567 in silico docking with CLusPro2.0 (30 different docking results) based on monomeric KD. An 'aggregate'
568 was mimicked using a region of the crystal lattice that had a similar structure as DAMMIF ab initio models
569 derived from SAXS data under conditions where KD was highly aggregated.

570 We arranged these models into three different 'pools' of structures from which best fitting multi-state
571 models were subsequently computationally selected (using FoXS). Pool 1: all monomeric and dimeric
572 models (44 models). Pool 2: monomer and only dimers found in our FGFR2^{pY1} crystal structures (7
573 models). Pool 3: As Pool 2, but also including trimers derived from our FGFR2^{pY1} crystal lattices (9

574 models). For JM-KD^{pY1} We prepared models similarly as for KD^{pY1}, using crystal-derived and in silico
575 docked dimeric and multimeric assemblies. Given that the long flexible JM region has a significant impact
576 on the SAXS pattern, we typically used five different JM conformations for the monomer and crystal-
577 lattice derived dimers, resulting in a pool of 55 different structures.

Mutation of FGFR2 proteins

579 Standard site-directed mutagenesis was carried out to mutate tyrosine residues into phenylalanine on KDs
580 to mimic the sequential phosphorylation pattern of KD (KD^{pY1} to KD^{pY6}; see schematic Fig. 1D and
581 Supplementary Fig. 2A. For the FGFR2 IIIb isoform this sequence is; pY657, pY587, pY467, pY589,
582 pY658 and pY734, adapted from the IIIc isoform(*30*)). The same methods were also used to mutate proline
583 residues on the C-terminal tail in this study.

In vitro dephosphorylation and phosphorylation of purified proteins

585 Calf Intestinal alkaline phosphatase (CIP, New England Biolabs) was conjugated on UltraLink Biosupport
586 beads (Thermo Fisher Scientific). CIP-beads were mixed with purified protein solution and rotated gently
587 at 4°C for overnight to remove phosphate group in solution. After dephosphorylation, protein solution and
588 CIP-beads were separated by centrifugation. Dephosphorylation level was examined by western blotting.
589 Purified FGFR2 proteins were phosphorylated by incubating with 5 mM ATP and 10 mM MgCl2. The
590 phosphorylation reactions were quenched by adding EDTA (prepared in 10 mM HEPES, pH 7.5) to a final
591 concentration of 100 mM. Proteins were analysed by SDS-PAGE and western blot to study the
592 phosphorylation status.

Transient cell transfection with plasmids

594 30 min before transfection, cells were harvested and resuspended in antibiotic-free medium. Transfection
595 was carried out using Metafectene (Biontex Cat#: T020) according to manufacturer manual.

Cell signalling studies

597 For mammalian cell studies, cells were starved for 16 hours, and left unstimulated or stimulated with
598 10ng/ml FGF7 ligand (R&D Systems Cat#: 251-KG/CF) at 37°C. After stimulation, medium was removed
599 and cells were put on ice and immediately lysed by scraping in ice-cold lysis buffer supplemented with
600 protease inhibitor (Calbiochem) and phosphatase inhibitor (1 mM sodium orthovanadate (NaVO3), and
601 10 mM sodium fluoride (NaF). Cells were cleared by centrifugation and the supernatants were subjected
602 to immunoblotting using the BioRad protein electrophoresis system. The intact gel was transfer to PVDF
603 membrane for probing with different antibodies. Phospho-protein blots were stripped with stripping buffer
604 (Millipore) and re-probed with total protein antibodies. Antibodies were from: Anti-Phospho-FGF
605 Receptor (Tyr653/654) Rabbit polyclonal, Cell Signaling Technology Cat#:3471; Anti-Phospho-FRS2-α
606 (Tyr436) Rabbit polyclonal, Cell Signaling Technology Cat#: 3861; Anti-Phospho-SHP-2 (Tyr542)
607 Rabbit polyclonal, Cell Signaling Technology Cat#: 3751; Anti-Phospho-Akt (Thr308) Rabbit
608 monoclonal, Cell Signaling Technology Cat#: 4056; Anti-Phospho-p44/42 MAPK (Erk1/2)
609 (Thr202/Tyr204) Rabbit monoclonal, Cell Signaling Technology Cat#: 4370; Anti-p44/42 MAPK
610 (Erk1/2) Rabbit monoclonal, Cell Signaling Technology Cat#: 4695; Anti-GRB2 Rabbit polyclonal, Cell
611 Signaling Technology Cat#: 3972; Anti-α-Tubulin Rabbit polyclonal, Cell Signaling Technology Cat#:
612 2144; Anti-GST Rabbit polyclonal, Cell Signaling Technology Cat#: 2622; Anti-FGFR2 Mouse
613 monoclonal, Santa Cruz Biotechnology Cat#: sc-6930; Anti-Phospho-Tyr Mouse monoclonal, Santa Cruz
614 Biotechnology Cat#: sc-7020; Anti-6xHis Mouse monoclonal, Takara Cat#: 631212.

Pulldown and western blots

For immunoblotting, proteins were separated by SDS-PAGE, transferred to PVDF membranes and incubated with the specific antibodies. Immune complexes were detected with horseradish peroxidase conjugated secondary antibodies and visualized by enhanced chemiluminescence reagent according to the manufacturer's instructions (Pierce). For pulldown experiments, 100ug of protein was prepared in 1 ml volume. MBP-tagged or GST-tagged proteins immobilized on Amylose beads (GE Healthcare Life Science) or Glutathione Sepharose (GE Healthcare Life Science) was added and incubated at 4°C overnight with gentle rotation. The beads were then spun down at 4,000 rpm for 3 minutes, supernatant was removed and the beads were washed with 1 ml lysis buffer. This washing procedure was repeated five times in order to remove non-specific binding. After the last wash, 50 µl of 2x Laemmli sample buffer were added, the sample was boiled and subjected to SDS-PAGE and western blot assays.

Fluorescence resonance energy transfer (FRET)

Recombinant GFP-JM-KD^{pY1}-CT^{C1} (donor) and RFP-JM-KD^{pY1}-CT^{C1} (acceptor) proteins (1µM) were used for *In vitro* steady-state FRET analysis. The changes of donor emission (510nm) upon dimer formation or dimer disruption upon the addition of CT were recorded at 25°C.

Quantitative imaging FRET microscopy

HEK293T cells 24 h after transfection were seeded onto coverslips and allowed to grow for a further 48 h then fixed by addition of 4% (w/vol) paraformaldehyde, pH 8.0, 20 min. at room temperature. Cells were then washed six or seven times with PBS, pH 8.0 and mounted onto a slide with mounting medium (0.1% p-phenylenediamine/ 75% glycerol in PBS at pH 7.5 – 8.0) and curated for 3 - 4 h before imaging. FLIM images were captured using a Leica SP5 II confocal microscope. Atto488 was excited at 900 nm with titanium–sapphire pumped laser (Mai Tai BB, Spectral Physics) with 710 - 920nm tunability and 70 femtosecond pulse width. Becker & Hickl (B&H) SPC830 data and image acquisition card was used for time-correlated single photon counting (TCSPC). Electrical time resolution 8 Pico seconds with a pixel resolution of 512 x 512. Data processing and analysis were done using B&H SPC FLIM analysis software. The fluorescence decays were fitted with a single exponential decay model.

Microscale thermophoresis (MST)

Binding affinities were measured using the Monolith NT.115 (NanoTemper Technologies, GmbH). Proteins were fluorescently labelled with Atto488 according to the manufacturer's protocol. Labelling efficiency was determined to be 1:1 (protein:dye) by measuring the absorbance at 280 and 488 nm. A 16 step dilution series of the unlabelled binding partner was prepared and mixed with the labelled protein at 1:1 ratio and loaded into capillaries. Measurements were performed at 25 °C in a buffer containing 20 mM HEPES, 150 mM NaCl, 1 mM TCEP and 0.01% Tween 20 at pH7.5. Data analysis was performed using Nanotemper Analysis software, v.1.2.101 and was plotted using Origin 7.0. All measurements were conducted as triplicates and the error bars were presented as the standard deviations of the triplicates. For the experiments employed to measure dimerization KD values are referred to a 'apparent' because, based on the differential concentrations, the fitting model assumes labelled are bound to unlabelled polypeptides.

Surface plasmon resonance (SPR)

SPR experiments were carried out using a BIAcore T100 instrument (GE Healthcare). CT^{C1} were immobilized on CM4 chips according to the standard amine coupling protocol. Briefly, carboxymethyl groups on the chip surface were activated with a 1:1 mixture of N-ethyl-N-(dimethyaminopropyl) carbodiimide (EDC) and N-hydroxysuccinimide (NHS). Proteins were diluted in 20 mM HEPES, pH 6.5 and injected over the activated chip surface. The unbound chip surface was blocked using ethanolamine. Proteins were immobilized to approximately 200 response units. Different concentrations of analytes were

659   injected over the immobilized chips at a flow rate of 30 μl/min. The sensor surface was regenerated by
660   injection of 30 μl of 0.1% SDS and 60 μl of 500 mM NaCl. Reference responses were subtracted from
661   flow cells for each analyte injection using BiaEvaluation software. The resulting sensorgrams were
662   anaylsed to determine the kinetic parameters. Raw data shows a rise in signal associated with binding
663   followed by a diminished signal after application of wash buffer.

Bio-layer interferometry (BLI)

665   BLI experiments were performed using a FortéBio Octet Red 384 using Anti-GST sensors. Assays were
666   done in 384 well plates at 25 °C. Association was measured by dipping sensors into solutions of analyte
667   protein (FGFR2 proteins) for 125 seconds and was followed by moving sensors to wash buffer for 100
668   seconds to monitor the dissociation process. Raw data shows a rise in signal associated with binding
669   followed by a diminished signal after application of wash buffer.

Peptides

671   ^{407}Juxtamembrane region^{462}, ^{407}KPDFSSQPAVHKLT^{420}, ^{414}PAVHKLTKRIPLRRQVT^{430},
672   ^{429}VTVSAESSSSMNSN^{442}, ^{439}MNSNTPLVRITTRL^{452}, ^{449}TTRLSSTADTPMLA^{462}, ^{801}PDPMPYEP^{808},
673   ^{801}PDPMPYEPCLPQYPH^{815}, ^{808}PCLPQYPHINGSVKT^{822}, ^{801}PDPMPYEPCLPQYPH^{815},
674   ^{808}PCLPQYPH^{815}, ^{808}PCLPQYPHINGS^{819}, ^{815}HINGSVKT^{822}, ^{804}MPYEPCLP^{811}. All peptides were
675   purchase from Genscript.

Supplementary Materials

Data and materials availability:

712 The accession number for the coordinate and structure for the mono-phosphorylated FGFR2 kinase
713 reported in this paper is PDB: 6V6Q.

References

718 1. C. M. Furdui, E. D. Lew, J. Schlessinger, K. S. Anderson, Autophosphorylation of FGFR1 Kinase
719   Is Mediated by a Sequential and Precisely Ordered Reaction. *Mol. Cell*. **21**, 711–717 (2006).
720 2. S. R. Hubbard, W. T. Miller, Receptor tyrosine kinases: mechanisms of activation and signaling.
721   *Curr. Opin. Cell Biol.* (2007), , doi:10.1016/j.ceb.2007.02.010.
722 3. S. Sarabipour, K. Hristova, Mechanism of FGF receptor dimerization and activation. *Nat.
723   Commun.* **7**, 10262 (2016).
724 4. C.-C. Lin, F. A. Melo, R. Ghosh, K. M. Suen, L. J. Stagg, J. Kirkpatrick, S. T. Arold, Z. Ahmed,
725   J. E. Ladbury, Inhibition of Basal FGF Receptor Signaling by Dimeric Grb2. *Cell*. **149**, 1514–
726   1524 (2012).
727 5. I. Maruyama, Mechanisms of Activation of Receptor Tyrosine Kinases: Monomers or Dimers.
728   *Cells*. **3**, 304–330 (2014).
729 6. N. F. Endres, R. Das, A. W. Smith, A. Arkhipov, E. Kovacs, Y. Huang, J. G. Pelton, Y. Shan, D.
730   E. Shaw, D. E. Wemmer, J. T. Groves, J. Kuriyan, Conformational Coupling across the Plasma
731   Membrane in Activation of the EGF Receptor. *Cell*. **152**, 543–556 (2013).
732 7. O. A. Karpov, G. W. Fearnley, G. A. Smith, J. Kankanala, M. J. McPherson, D. C. Tomlinson, M.
733   A. Harrison, S. Ponnambalam, Receptor tyrosine kinase structure and function in health and
734   disease. *AIMS Biophys.* **2**, 476–502 (2015).
735 8. A. Östman, Regulation of receptor tyrosine kinase signaling by protein tyrosine phosphatases.
736   *Trends Cell Biol.* **11**, 258–266 (2001).
737 9. X. Zhang, J. Gureasko, K. Shen, P. A. Cole, J. Kuriyan, An Allosteric Mechanism for Activation
738   of the Kinase Domain of Epidermal Growth Factor Receptor. *Cell*. **125**, 1137–1149 (2006).
739 10. M. A. Lemmon, J. Schlessinger, Cell signaling by receptor tyrosine kinases. *Cell*. **141**, 1117–34
740   (2010).
741 11. R. M. Baxter, J. P. Secrist, R. R. Vaillancourt, A. Kazlauskas, Full Activation of the Platelet-
742   derived Growth Factor β-Receptor Kinase Involves Multiple Events. *J. Biol. Chem.* **273**, 17050–
743   17055 (1998).
744 12. L. E. Wybenga-Groot, B. Baskin, S. H. Ong, J. Tong, T. Pawson, F. Sicheri, Structural Basis for

Autoinhibition of the EphB2 Receptor Tyrosine Kinase by the Unphosphorylated Juxtamembrane Region. *Cell*. **106**, 745–757 (2001).

13. R. Herbst, S. J. Burden, The juxtamembrane region of MuSK has a critical role in agrin-mediated signaling. *EMBO J.* **19**, 1167–1167 (2000).

14. J. H. Till, M. Becerra, A. Watty, Y. Lu, Y. Ma, T. A. Neubert, S. J. Burden, S. R. Hubbard, Crystal Structure of the MuSK Tyrosine Kinase. *Structure*. **10**, 1187–1196 (2002).

15. J. Griffith, J. Black, C. Faerman, L. Swenson, M. Wynn, F. Lu, J. Lippke, K. Saxena, The Structural Basis for Autoinhibition of FLT3 by the Juxtamembrane Domain. *Mol. Cell*. **13**, 169–178 (2004).

16. S. R. Hubbard, Juxtamembrane autoinhibition in receptor tyrosine kinases. *Nat. Rev. Mol. Cell Biol.* **5**, 464–471 (2004).

17. C. D. Mol, D. R. Dougan, T. R. Schneider, R. J. Skene, M. L. Kraus, D. N. Scheibe, G. P. Snell, H. Zou, B.-C. Sang, K. P. Wilson, Structural Basis for the Autoinhibition and STI-571 Inhibition of c-Kit Tyrosine Kinase. *J. Biol. Chem.* **279**, 31655–31663 (2004).

18. N. Jura, N. F. Endres, K. Engel, S. Deindl, R. Das, M. H. Lamers, D. E. Wemmer, X. Zhang, J. Kuriyan, Mechanism for activation of the EGF receptor catalytic domain by the juxtamembrane segment. *Cell*. **137**, 1293–307 (2009).

19. K. W. Thiel, G. Carpenter, Epidermal growth factor receptor juxtamembrane region regulates allosteric tyrosine kinase activation. *Proc. Natl. Acad. Sci.* **104**, 19238–19243 (2007).

20. L. M. Shewchuk, A. M. Hassell, B. Ellis, W. D. Holmes, R. Davis, E. L. Horne, S. H. Kadwell, D. D. McKee, J. T. Moore, Structure of the Tie2 RTK domain: self-inhibition by the nucleotide binding loop, activation loop, and C-terminal tail. *Structure*. **8**, 1105–13 (2000).

21. C. M. Chang, H. K. Shu, L. Ravi, R. J. Pelley, H. Shu, H. J. Kung, A minor tyrosine phosphorylation site located within the CAIN domain plays a critical role in regulating tissue-specific transformation by erbB kinase. *J. Virol.* **69**, 1172–80 (1995).

22. M. Landau, S. J. Fleishman, N. Ben-Tal, A Putative Mechanism for Downregulation of the Catalytic Activity of the EGF Receptor via Direct Contact between Its Kinase and C-Terminal Domains. *Structure*. **12**, 2265–2275 (2004).

23. E. R. Wood, A. T. Truesdale, O. B. McDonald, D. Yuan, A. Hassell, S. H. Dickerson, B. Ellis, C. Pennisi, E. Horne, K. Lackey, K. J. Alligood, D. W. Rusnak, T. M. Gilmer, L. Shewchuk, A Unique Structure for Epidermal Growth Factor Receptor Bound to GW572016 (Lapatinib). *Cancer Res.* **64**, 6652–6659 (2004).

24. K. S. Gajiwala, EGFR: Tale of the C-terminal tail. *Protein Sci.* **22**, 995–999 (2013).

25. T. Ueda, H. Sasaki, Y. Kuwahara, M. Nezu, T. Shibuya, H. Sakamoto, H. Ishii, K. Yanagihara, K. I. Mafune, M. Makuuchi, M. Terada, Deletion of the carboxyl-terminal exons of K-sam/FGFR2 by short homology-mediated recombination, generating preferential expression of specific messenger RNAs. *Cancer Res.* **24**, 6080–6 (1999).

26. I. Bernard-Pierrot, D. Ricol, A. Cassidy, A. Graham, P. Elvin, A. Caillault, S. Lair, P. Broët, J.-P. Thiery, F. Radvanyi, Inhibition of human bladder tumour cell growth by fibroblast growth factor receptor 2b is independent of its kinase activity. Involvement of the carboxy-terminal region of the receptor. *Oncogene*. **23**, 9201–9211 (2004).

27. X. Li, Y. Hou, T. Shi, Y. He, D. Ren, Z. Song, S. Wei, G. Chen, J. Chen, S. Xu, Clinicopathological characteristics and genetic analysis of pulmonary carcinoid tumors: A single-center retrospective cohort study and literature review. *Oncol. Lett.* **19**, 2446–2456 (2020).

28. P. K.-S. Ng, J. Li, K. J. Jeong, S. Shao, H. Chen, Y. H. Tsang, S. Sengupta, Z. Wang, V. H. Bhavana, R. Tran, S. Soewito, D. C. Minussi, D. Moreno, K. Kong, T. Dogruluk, H. Lu, J. Gao,

791   C. Tokheim, D. C. Zhou, A. M. Johnson, J. Zeng, C. K. M. Ip, Z. Ju, M. Wester, S. Yu, Y. Li, C.
792   P. Vellano, N. Schultz, R. Karchin, L. Ding, Y. Lu, L. W. T. Cheung, K. Chen, K. R. Shaw, F.
793   Meric-Bernstam, K. L. Scott, S. Yi, N. Sahni, H. Liang, G. B. Mills, Systematic Functional
794   Annotation of Somatic Mutations in Cancer. *Cancer Cell*. **33**, 450-462.e10 (2018).

795   29.   I. Gudernova, L. Balek, M. Varecha, J. F. Kucerova, M. Kunova Bosakova, B. Fafilek, V.
796   Palusova, S. Uldrijan, L. Trantirek, P. Krejci, Inhibitor repurposing reveals ALK, LTK, FGFR,
797   RET and TRK kinases as the targets of AZD1480. *Oncotarget*. **8**, 109319–109331 (2017).

798   30.   H. Chen, C. F. Xua, J. Ma, A. V. Eliseenkova, W. Li, P. M. Pollock, N. Pitteloud, W. T. Miller,
799   T. A. Neubert, M. Mohammadi, A crystallographic snapshot of tyrosine trans-phosphorylation in
800   action. *Proc. Natl. Acad. Sci. U. S. A.* (2008), doi:10.1073/pnas.0807752105.

801   31.   J. H. Bae, J. Schlessinger, Asymmetric tyrosine kinase arrangements in activation or
802   autophosphorylation of receptor tyrosine kinases. *Mol. Cells*. **29**, 443–448 (2010).

803   32.   S. H. Ong, G. R. Guy, Y. R. Hadari, S. Laks, N. Gotoh, J. Schlessinger, I. Lax, FRS2 Proteins
804   Recruit Intracellular Signaling Pathways by Binding to Diverse Targets on Fibroblast Growth
805   Factor and Nerve Growth Factor Receptors. *Mol. Cell. Biol.* **20**, 979–989 (2000).

806   33.   Z. Ahmed, A. C. Schüller, K. Suhling, C. Tregidgo, J. E. Ladbury, Extracellular point mutations
807   in FGFR2 elicit unexpected changes in intracellular signalling. *Biochem. J.* **413**, 37–49 (2008).

808   34.   H. R. Burgar, H. D. Burns, J. L. Elsden, M. D. Lalioti, J. K. Heath, Association of the Signaling
809   Adaptor FRS2 with Fibroblast Growth Factor Receptor 1 (Fgfr1) Is Mediated by Alternative
810   Splicing of the Juxtamembrane Domain. *J. Biol. Chem.* **277**, 4018–4023 (2002).

811   35.   Z. Ahmed, R. George, C.-C. Lin, K. M. Suen, J. A. Levitt, K. Suhling, J. E. Ladbury, Direct
812   binding of Grb2 SH3 domain to FGFR2 regulates SHP2 function. *Cell. Signal.* **22**, 23–33 (2010).

813   36.   Z. Ahmed, C.-C. Lin, K. M. Suen, F. A. Melo, J. A. Levitt, K. Suhling, J. E. Ladbury, Grb2
814   controls phosphorylation of FGFR2 by inhibiting receptor kinase and Shp2 phosphatase activity.
815   *J. Cell Biol.* **200**, 493–504 (2013).

816   37.   K. S. Gajiwala, K. Maegley, R. A. Ferre, Y. A. He, X. Yu, Ack1: Activation and Regulation by
817   Allostery. *PLoS One* (2013), doi:10.1371/journal.pone.0053994.

818   38.   Z. Timsah, Z. Ahmed, C.-C. Lin, F. A. Melo, L. J. Stagg, P. G. Leonard, P. Jeyabal, J. Berrout, R.
819   G. O'Neil, M. Bogdanov, J. E. Ladbury, Competition between Grb2 and Plcγ1 for FGFR2
820   regulates basal phospholipase activity and invasion. *Nat. Struct. Mol. Biol.* **21**, 180–188 (2014).

821   39.   H. Chen, Z. Huang, K. Dutta, S. Blais, T. A. Neubert, X. Li, D. Cowburn, N. J. Traaseth, M.
822   Mohammadi, Cracking the Molecular Origin of Intrinsic Tyrosine Kinase Activity through
823   Analysis of Pathogenic Gain-of-Function Mutations. *Cell Rep.* **4**, 376–384 (2013).

824
825
826
827
828
829
830
831
832
833
834
835
836
837

838 **Figures**

Figure 1
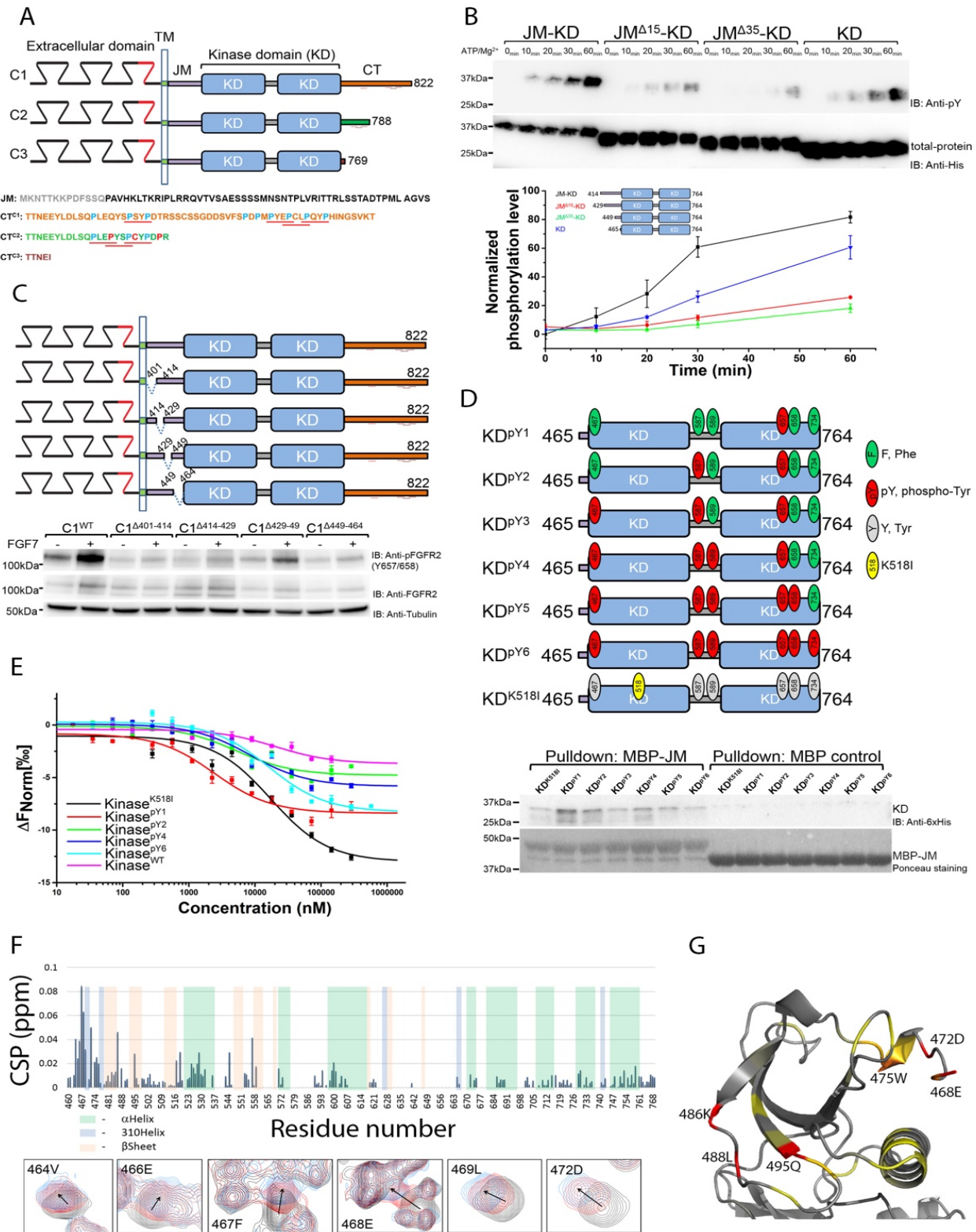
Fig. 1. The presence of JM enhances activity of KD. (**A**) Schematic diagram of FGFR2IIIb C1, C2, and C3 isoform. These isoforms differ only in their C-terminal tail. C1 isoform (orange) includes the full length C-terminal tail (CT^{C1}); C2 isoform (green) has a truncated C-terminal tail (CT^{C2}) and also includes three point mutations (red); the C3 isoform (purple) is truncated by 56 residues (CT^{C3}). Proline residues are shown (blue) and proline-rich motifs in C1 and C2 isoforms are underlined. JM sequence is also shown (black) – membrane-bound sequence of JM (grey). (**B**) *In vitro* kinase assay using progressive JM-deletions in JM-KD (residues 414-764, black; 431-764, red; 447-764, green; and 465-764, blue). 100 nM of each protein was used for the *in vitro* phosphorylation assay (see STAR Methods for details). Phosphorylation levels were determined using a general pY99 antibody. His-tag antibody was used for total protein control. (**C**) Intermittent deletions in JM down-regulate FGFR2 activity. HEK293T cells were transfected with FGFR2 with JM deletions ($C1^{\Delta401-414}$, $C1^{\Delta414-429}$, $C1^{\Delta429-449}$, and $C1^{\Delta449-464}$). Cells were serum starved overnight and left unstimulated or stimulated with 10ng/ml FGF7 for 15 min. Cell lysates were blotted with indicated antibodies. (**D**) Binding of JM to progressively phosphorylated KD. Six tyrosine residues on KD were mutated to mimic the sequential phosphorylation pattern of KD (KD^{pY1} to KD^{pY6}; fig. S1A). MBP-JM was used to pulldown KDs (His-tagged). (**E**) MST measurements of the binding affinity between JM and KD with different phosphorylation levels. JM was labelled with Atto 488 dye and serial dilutions of KD were titrated at 25˚C. (**F**) CSPs of ^{15}N-KD^{pY1} titrated by JM derived from ^{1}H-^{15}N HSQC spectra (fig. S1E). Large changes occur on the N-terminal lobe. Selected residues experiencing major CSPs are shown as the bottom panels. (**G**) CSPs from residues in ^{15}N-KD^{pY1} as JM is titrated plotted on the structure of KD^{pY1}. CSPs shown as gradient: Yellow – lower, Red - higher. Selected residues with major CSPs are labelled.

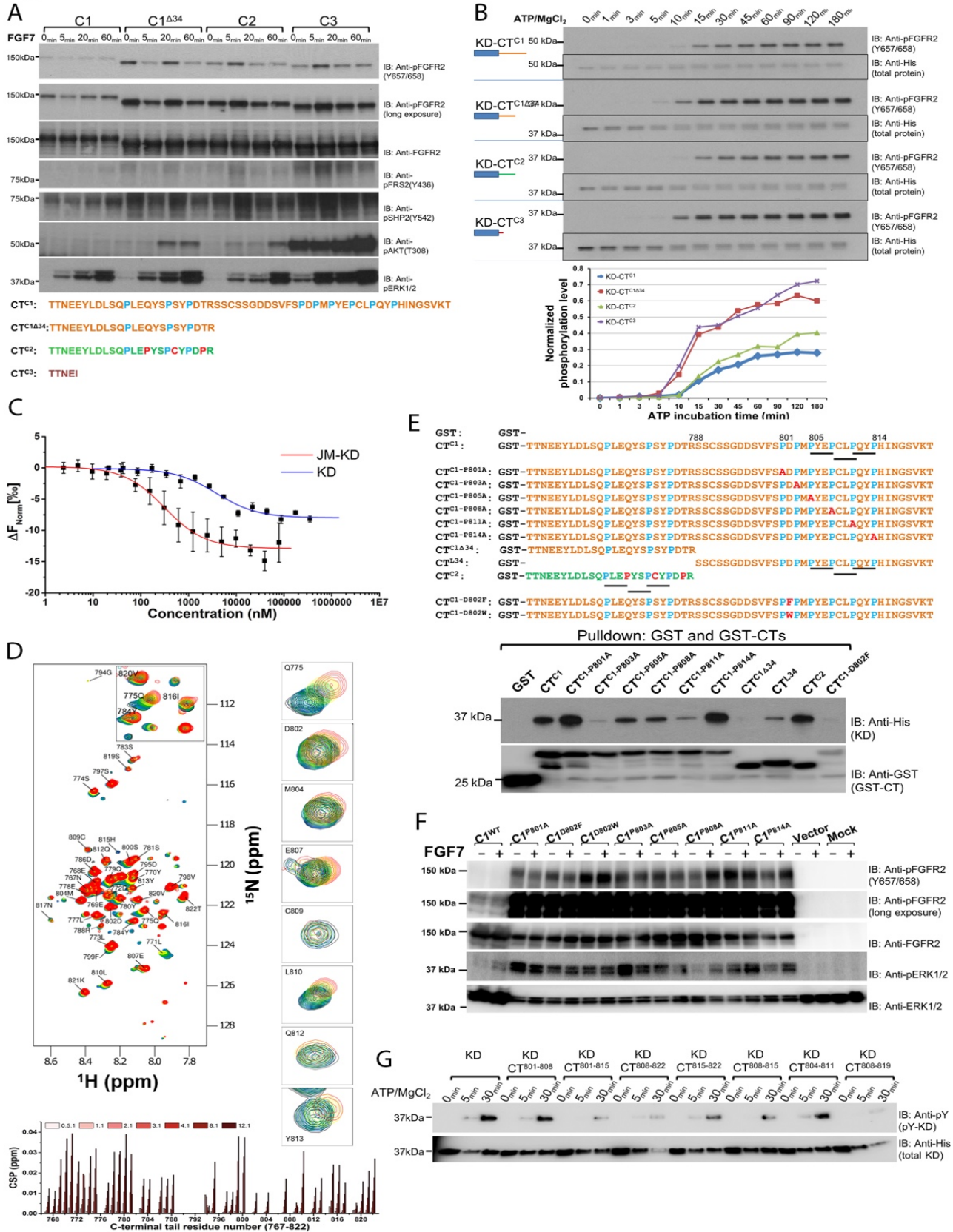## Figure 2
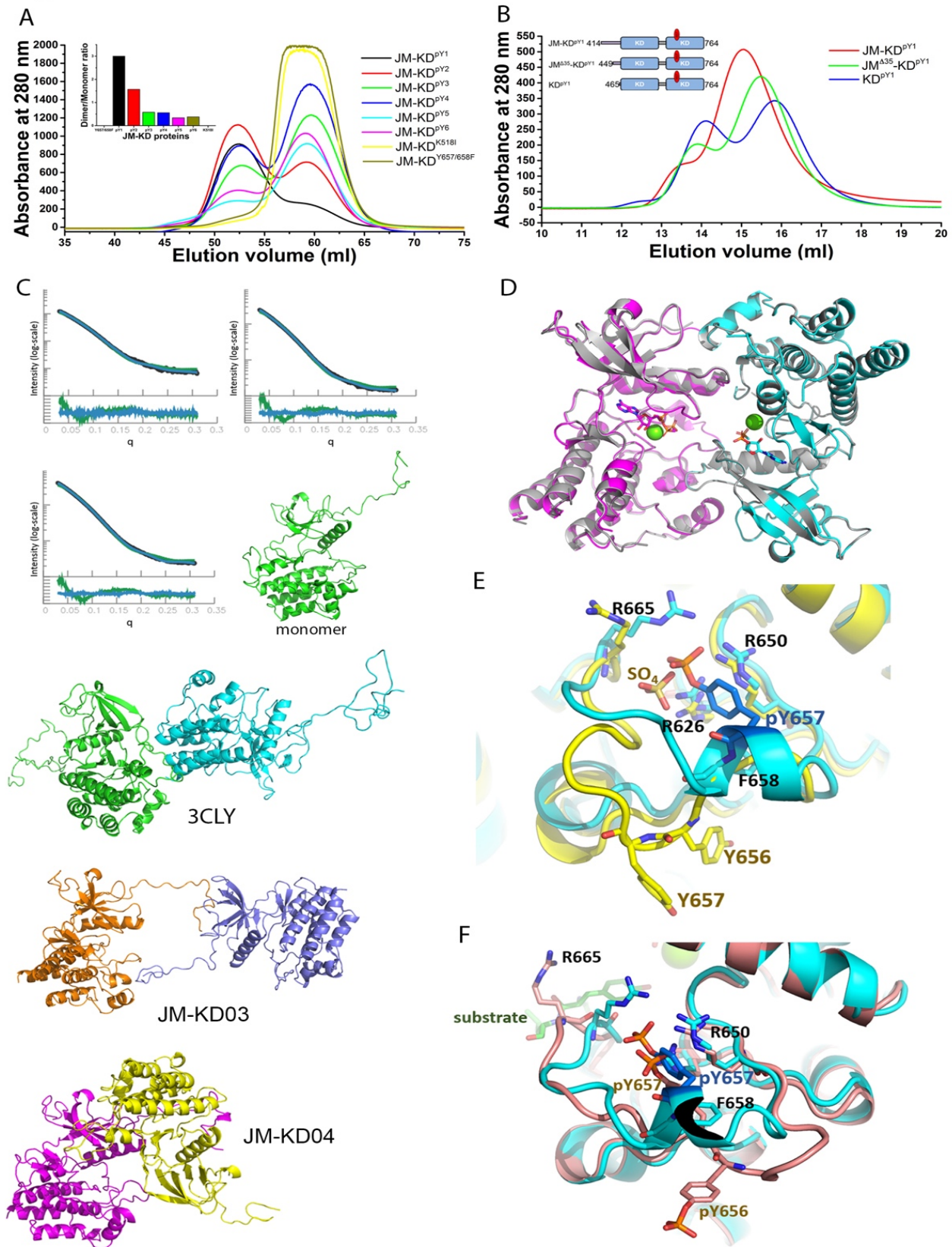
Fig. 2. JM forms an intermolecular interaction in an asymmetric KD dimer. (A) JM-KD construct with progressively increasing pY residues on KD were run on size exclusion chromatography (SEC) at 60 - 80 µM (inset: dimer/monomer ratio of KD with different phosphorylation levels). (**B**) Dimerization of KD^{pY1} is reduced in the presence of JM. The dimerization of JM-KD^{pY1} constructs with JM deletions (JM-KD^{pY1}; $JM^{\Delta 35}$-KD^{pY1}; and KD^{pY1}) was determined using 10 µM injected on a size exclusion column. (**C**) SAXS description of the structure of JM-KD^{pY1}. Top panel: the calculated SAXS pattern for 1-state (green) and 3-state (blue) models fitted to the experimental data (black) at different total KD concentrations (left plot, 65 µM; middle, 130 µM and right 210 µM); bottom panel: residuals of fit for 1-state (green) and 3-state models (blue). The resolution, q, is given in 1/Å and the intensity is given in arbitrary units. Model structures based on crystal structure-derived and *in silico*-docked dimeric and multimeric assemblies. Mono – structure of the monomeric state, JM-KD03 - two kinases (orange/blue) loosely connected through their JM interactions; JM-KD04 asymmetric dimer where JM of the enzyme-like state (magenta) binds to the substrate-and cyan). (**D**) Asymmetric unit of KD^{pY1} containing four molecules. Phosphorylated chains A (magenta) and C (cyan) superimposed onto chains C and D (grey). ATP shown as stick model, and Mg^{2+} as green sphere. (**E**) A-loop superposition between KD^{pY1} (chain B, cyan) and unphosphorylated kinase with 2PSQ (chain A, yellow). (**F**) Zoom into the A-loop between KD^{pY1} (chain B) and dephosphorylated kinase with 2PVF (salmon).

Figure 3

CT^C1: TTNEEYLDLSQPLEQYSPSYPDTRSSCSSGDDSVFSPDPMPYEPCLPQYPHINGSVKT

CT^C1Δ34: TTNEEYLDLSQPLEQYSPSYPDTR

CT^C2: TTNEEYLDLSQPLEPYSPCYPDPR

CT^C3: TTNEI

Fig. 3. Proline-rich motifs interact and downregulate kinase activity. (**A**) Immunoblotting analysis of signalling activity of FGFR2IIIb isoforms. FGFR2^{C1}; FGFR2$^{C1\Delta34}$; FGFR2^{C2} and FGFR2^{C3} were transfected into HEK293T cells. Cells were starved or stimulated with 10ng/ml FGF7. The levels of receptor phosphorylation and downstream activity on each isoform were probed with the indicated antibodies. (**B**) Proline-rich CT inhibits *in vitro* kinase activity. Recombinant KD-CT^{C1}, KD-CT^{C2}, KD-CT^{C3} and control clone: KD-CT$^{C1\Delta34}$ were incubated with ATP/Mg^{2+} at 25 °C and quenched with 100 mM EDTA at different time points as indicated. The activation level was measured using an anti-pY657/658 antibody. Bottom: The densitometry analysis of kinase activity (KD-CT^{C1} – blue; KD-CT^{C2} – green; KD-CT^{C3} – purple and KD-CT$^{C1\Delta34}$ – red). (**C**) The affinities of CT^{C1} to JM-KD^{pY1} (red) and KD^{pY1} (blue) determined using MST. CT^{C1} was labelled with Atto488 dye then titrated with unlabelled JM-KD^{pY1} and KD^{pY1}. (**D**) HSQC spectra of unbound ^{1}H-^{15}N-labelled CT^{C1} overlaid with KD^{pY1}-bound CT^{C1} at different ratio (black (0:1) to red (12:1)). Examples of peaks with high chemical-shift perturbations (CSPs) are shown by labels indicating the assignment of given peaks. CSPs chat of ^{15}N-KD^{pY1} titrated by CT^{C1} was derived from ^{1}H-^{15}N HSQC spectra. Large changes occur on both N-terminal and C-terminal residues of CT^{C1}. (**E**) Wild type GST-CT^{C1} and its individual P to A mutants , the first 24 residues of CT (CT$^{C1\Delta34}$), the last 34 residues (CT^{L34}), CT^{C2} and CT^{C1} D802F or D802W (to explore the importance of the charged acid group in binding) were used for a GST pulldown experiment with KD^{pY1}. The symmetric dimerization of KD^{pY1} at the concentration range used in this experiment (1 µM) was assumed to have negligible impact on binding of the various CT variants. (**F**) The presence of the intact proline-rich motif in FGFR2^{C1} inhibits both FGFR2 and downstream ERK1/2 activities. FGFR2^{C1} variants with individual P/A, D/F, and D/W mutants as indicated were transfected into HEK293T cells. Cells were starved or stimulated with 10ng/ml FGF7 for 15 minutes. Cell lysates were blotted with indicated antibodies to examine the importance of the proline-rich sequence on CT. (**G**) Dephosphorylated KD was incubated with seven CT-derived short peptides including fragments of the proline-rich sequences (residues 801-808; 801-815; 808-822; 815-822; 808-815; 804-811 and 808-819) to test their ability to regulate kinase activity. See STAR Methods for phosphorylation and quenching procedures.
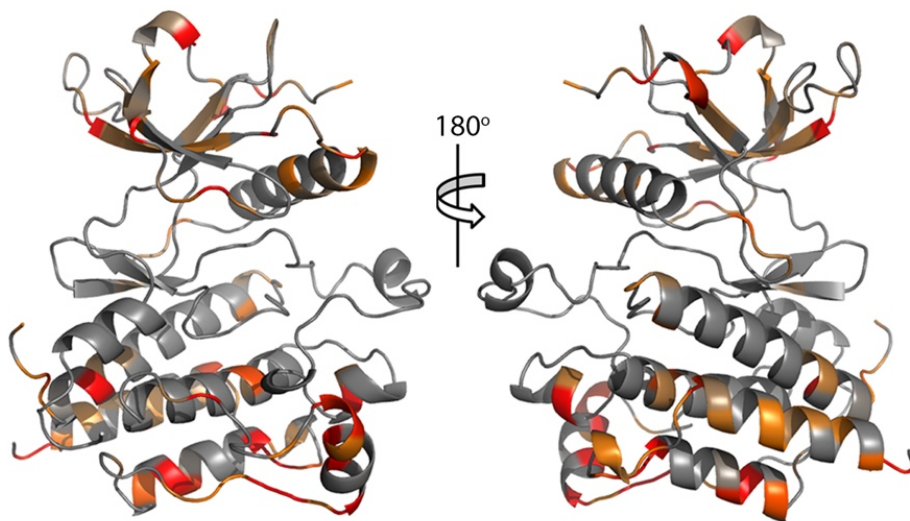
Figure 4

A

B
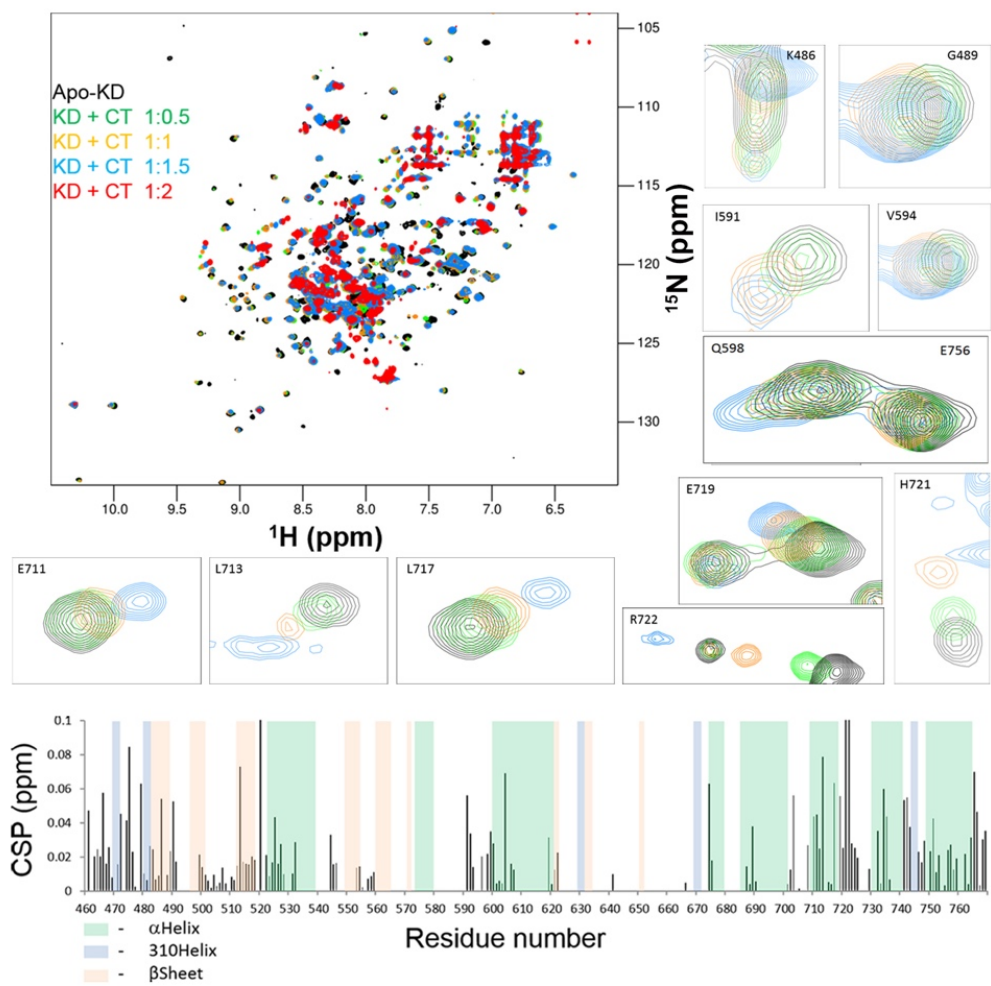
Fig. 4. Identification of CT binding site on KD using NMR. (**A**) ^{1}H-^{15}N HSQC spectra of unbound FGFR2 KD^{pY1} (Black) overlaid with CT^{C1} bound KD^{pY1} at different concentration ratios. Examples of peaks with major CSPs shown. CSPs chart of CT^{C1} titrated into ^{15}N-KD^{pY1} derived from ^{1}H-^{15}N HSQC spectra. Large CSPs are observed at both N-terminal and C-terminal lobes. (**B**) CSPs of CT^{C1} binding to KD^{pY1} plotted on the X-ray structure of mono-phosphorylated kinase. As shown in Fig. 1G, a red-to-yellow gradient was used to indicate the CSP residues. Minor CSPs appear on one side of the regulatory αC helix, suggesting the binding of JM could regulate kinase activity.
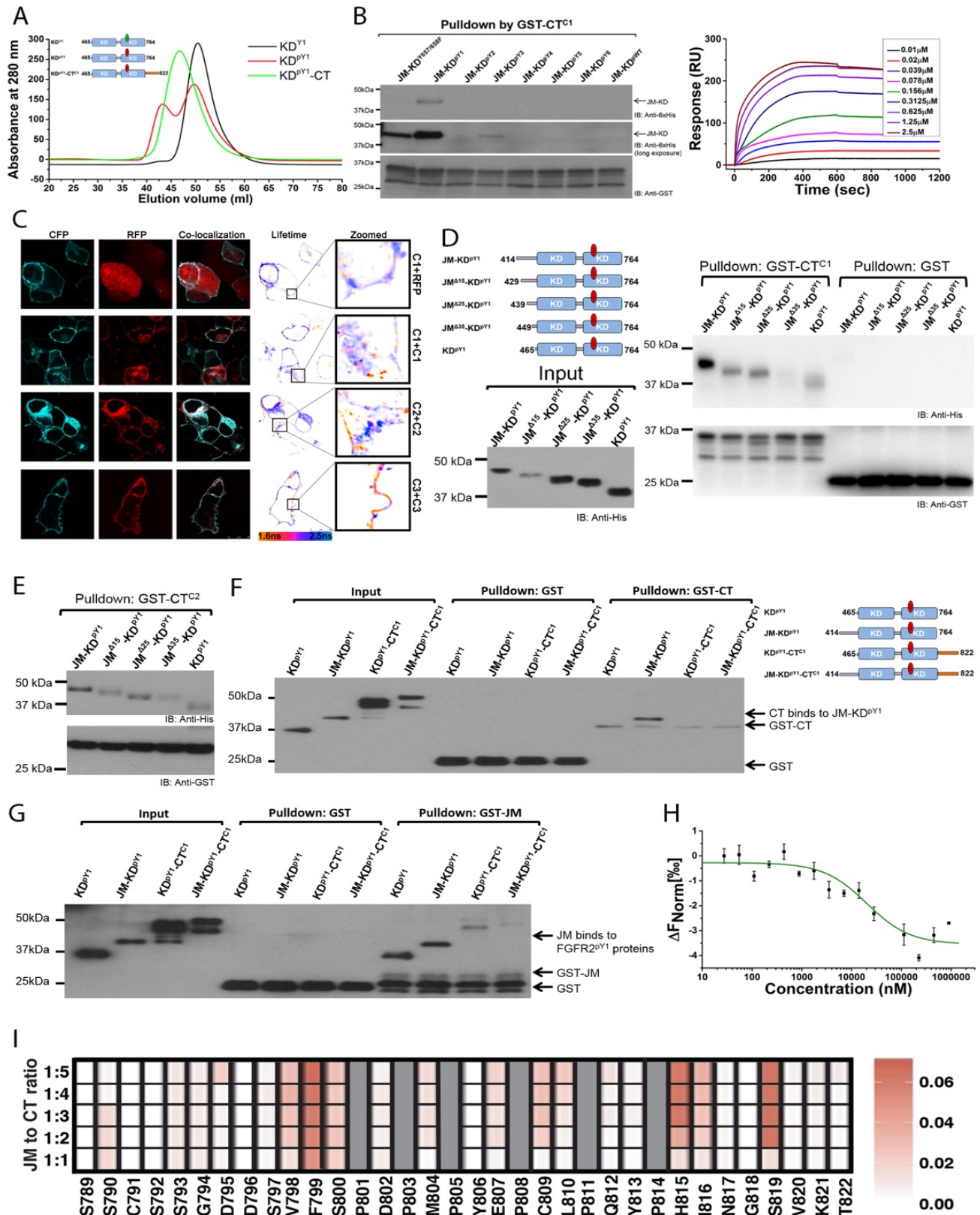
# Figure 5

Fig. 5. CT binding to KD^{pY1} disrupts the formation of asymmetric dimer. (**A**) Dimerization status of FGFR2 kinases in the presence or absence of CT. KD^{pY1} (blue curve) includes a dominant population of dimers at 60 μM in SEC, whereas the unphosphorylated KD (green curve) prevails as a monomer. The mono-phosphorylated KD^{pY1}-CT construct (red curve) also exists as a monomer in solution. (**B**) Phosphorylation of JM-KD affects CT binding. GST-CT^{C1} was used to pulldown the progressively increasing phosphorylation of JM-KD constructs. The pulldown indicates that JM-KD^{pY1} was the best binding partner for GST-CT^{C1}. (**C**) Dimerization of FGFR2. FLIM analysis of the FRET between the FGFR2-CFP and FGFR2-RFP. First panel: Reference lifetime measurements between FGFR2-GFP and RFP-alone, control for no interaction. The mean lifetime is centred around ~2.1 ns (Blue), which corresponds to the mean lifetime for isolated CFP alone. Second panel: Dimerization of C1 showing a measurable left shift with of the molecule showing FRET above the control. Note that most interactions are seen in the intracellular vesicles. Third panel: Dimerization of C2. 16% of molecules on plasma membrane showing dimerization above the control threshold (Orange). Forth panel: Dimerization of C3, as with C1, 26% of the molecules are showing interaction (Orange) however unlike C1, almost all of the interactions are on the plasma membrane. Inserts with arrows showing exquisite separation of dimeric and non-dimeric FGFR2-C3 on the plasma membrane. (**D**) GST-CT^{C1} was used to pull down five mono-phosphorylated constructs of JM-KD^{pY1} with progressively truncated JM (JM-KD^{pY1}, JM^{Δ15}-KD^{pY1}, JM^{Δ25}-KD^{pY1}, JM^{Δ35}-KD^{pY1}, and KD^{pY1}). The presence of the intact JM enhances the interaction with GST-CT^{C1}. (**E**) GST-CT^{C2} was used to pull down five mono-phosphorylated constructs of JM-KD^{pY1} as described in Fig. 6D. The presence of the intact JM also enhances the interaction with the CT from C2 isoform. (**F**) A GST-CT^{C1} pulldown of different FGFR2IIIb mono-phosphorylated proteins that include the presence or absence of JM and/or CT (KD^{pY1}; JM-KD^{pY1}; KD^{pY1}-CT, and JM-KD^{pY1}-CT), shows that the presence of JM, but not CT, promotes the interaction between kinase domain and GST-CT^{C1}. The presence of CT inhibits the GST-CT^{C1} interaction, indicating CT binds through an intramolecular interaction. (**G**) A GST-JM pulldown of different FGFR2IIIb mono-phosphorylated proteins (as described in Fig. 5F), shows that the presence of JM does not block JM binding suggesting that JM of one protomer binds to the other in the mono-phosphorylated dimers (previously identified for KD and JM-KD). The latch to the protomer in the asymmetric dimer leaves an available JM binding site. The presence of CT (in KD-CT^{C1} and JM-KD^{pY1}-CT^{C1}) reduces JM binding. (**H**) MST measurement of JM binding to CT. A two-fold serial dilution of CT was titrated into JM which was labelled with Atto 488. (**I**) NMR titration of JM titrated into ^{15}N-labelled CT using a red-to-white gradient, where white represents the weakest CSP and red depicts the strongest CSP. Proline residues are not visible in this experiment (shown in grey).

Figure 6
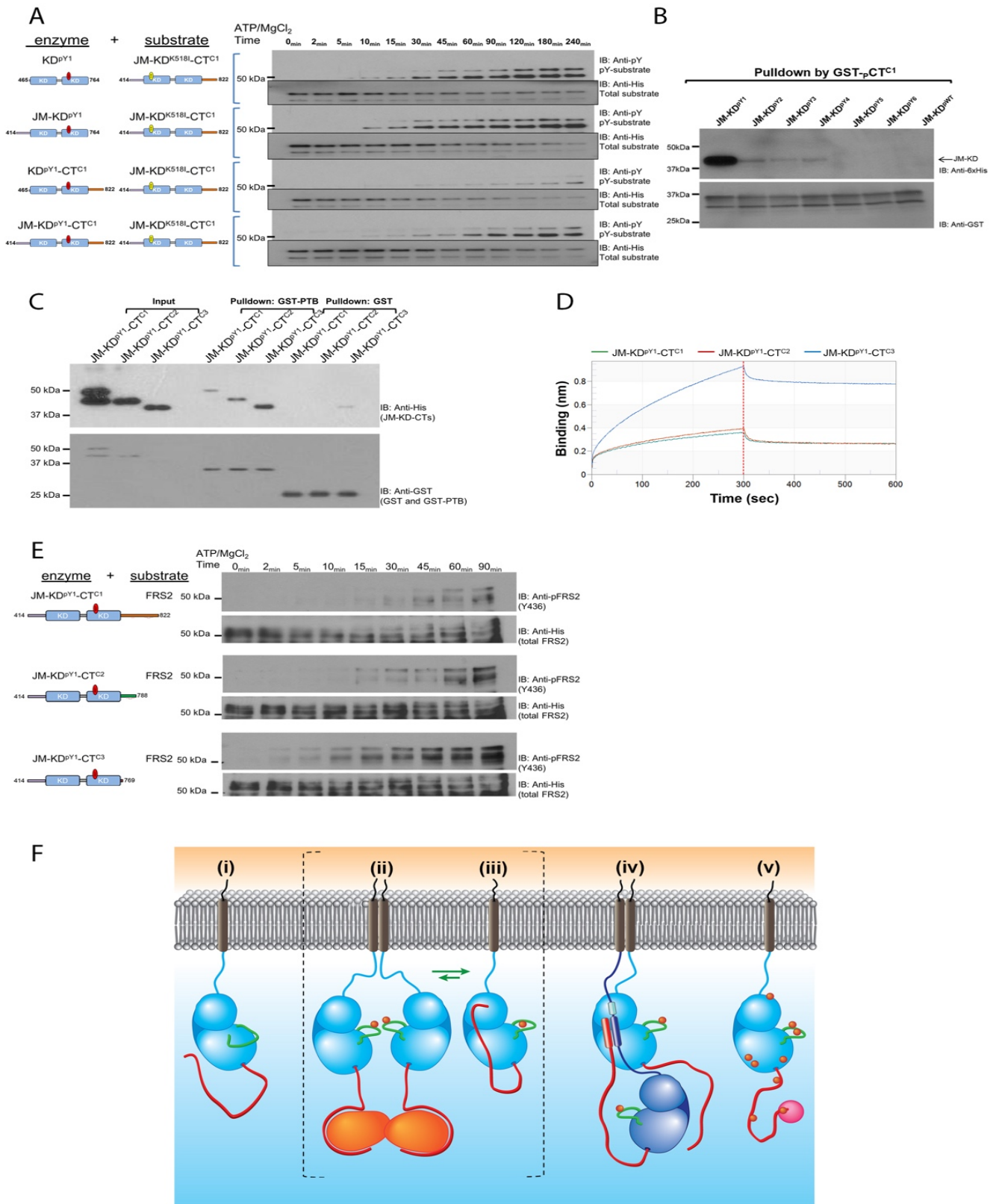
1088 **Fig. 6. JM and CT combine to regulate KD.** (**A**) Kinase activity is controlled by both JM and CT.
1089 KD^{pY1}, JM-KD^{pY1}, KD^{pY1}-CT^{C1}, and JM-KD^{pY1}-CT^{C1}, were incubated with kinase-dead JM-KD^{K518I}-
1090 CT^{C1} in a 1:1000 ratio in the presence of ATP/Mg^{2+} and quenched with EDTA at different time points as
1091 indicated. The phosphorylation of JM-KD^{K518I}-CT^{C1} was measured using a pY99 antibody. (**B**)
1092 Phosphorylation of CT (pCT^{C1}) reduces its binding to KD with higher phosphorylation order. GST-CT^{C1}
1093 was phosphorylated by JM-KD^{WT}-CT^{C1} and used for a GST pulldown assay with different phosphorylated
1094 JM-KD (JM-KD^{pY1} – JM-KD^{pY6} and wild type JM-KD). (**C**) GST-FRS2 PTB domain was used precipitate
1095 the following His-tagged constructs representing the mono-phosphorylated isoforms of FGFR2IIIb; JM-
1096 KD^{pY1}-CT^{C1}, JM-KD^{pY1}-$CT^{C2}$and JM-KD^{pY1}-CT^{C3}. The presence of the intact CT in the C1 isoform
1097 inhibits the interaction of FRS2 with its cognate site on JM. (**D**) BLI measurement of GST-FRS2 PTB
1098 binding to JM-KD^{pY1}-CT^{C1}, JM-KD^{pY1}-$CT^{C2}$and JM-KD^{pY1}-CT^{C3}. The GST-PTB domain from FRS2 was
1099 immobilised on the sensor and was exposed to 2.6 µM of the cytoplasmic region of each of the FGFR2
1100 isoforms. After 300 s the chip was washed. The sensorgrams clearly show that over the time course up to
1101 300 seconds (prior to the washing step; dotted line), in the absence of CT (C3 isoform) a significantly
1102 increased amount of FGFR2 protein binds to the PTB domain compared with the C1 and C2 isoforms. (**E**)
1103 The FGFR2 isoforms (JM-KD^{pY1}-CT^{C1}, JM-KD^{pY1}-CT^{C2} and JM-KD^{pY1}-CT^{C3}) were incubated with FRS2
1104 protein in a 1:100 ratio in the presence of ATP/Mg^{2+} and quenched at different time points as indicated.
1105 The phosphorylation of FRS2 was measured using an anti-pFRS2 (Y436) antibody. (**F**) i: In the absence
1106 of stimulation the unphosphorylated FGFR2 (light blue, JM light blue line, CT red line) can exist as a
1107 monomer freely diffusing through the plasma membrane. ii: Random collision of FGFR2 results in dimer
1108 formation. Dimeric GRB2 (orange) is recruited via a proline-rich sequence on CT into a heterotetramer.
1109 This stabilizes the mono-phosphorylated active A-loop (green line) tyrosine residues (red circles) on KD,
1110 but signalling is stalled by the presence of GRB2 on CT. iii: the mono-phosphorylated KD provides a
1111 strong binding site for CT. CT to KD^{pY1} interaction results in the releasing of GRB2. This interaction
1112 inhibits the JM-mediated formation of asymmetric dimer and thus prevents the KD^{pY1} intermediate state
1113 from further auto-phosphorylation activity. Active intermediate states ii: and iii: are in equilibrium, the
1114 presence of the states is dependent on GRB2 concentration and hence the ability of GRB2 to compete with
1115 the intramolecular interaction with KD for binding to CT. iv: Binding of extracellular growth factor co-
1116 localizes two receptors and permits the formation the active, asymmetric dimeric conformation. This is
1117 sustained by the interaction of JM from the enzyme-like receptor (dark blue) with KD of the substrate-
1118 like receptor (light blue). The sequence on JM which binds to KD (light blue thick line) is immediately
1119 proximal to a sequence (dark blue thick line) which binds in an independent interaction to CT of the
1120 enzyme-like receptor. This binding site (red thick line) includes the proline-rich motif that recognizes a
1121 site on KD and GRB2. Thus, JM-CT interaction blocks auto-inhibition and GRB2 recruitment. This
1122 ensures that the active state is prolonged. In this conformation the CT of the substrate-like receptor can
1123 access the enzyme-like KD active site. v: Prolonged activity of the dynamic asymmetric dimer results in
1124 increasing phosphorylation of KD and CT. As the pY burden increases the dimerization between KDs
1125 reduces until they fully dissociate. The phosphorylated KD abrogates the inhibitory intramolecular binding
1126 of CT and the recruitment of GRB2. The receptor is therefore available for recruitment of downstream
1127 effector proteins (magenta).
1128
1129
1130
1131

1   **Supplementary Materials**
2
3   **Title**
4   Regulation of kinase activity by combined action of juxtamembrane and C-terminal
5   **Authors**

6   Chi-Chuan Lin[1], Lukasz Wieteska[1], Guillaume Poncet-Montange[2], Kin M. Suen[1], Stefan T.
7   Arold[3,4], Zamal Ahmed[5], John E. Ladbury[1]*
8
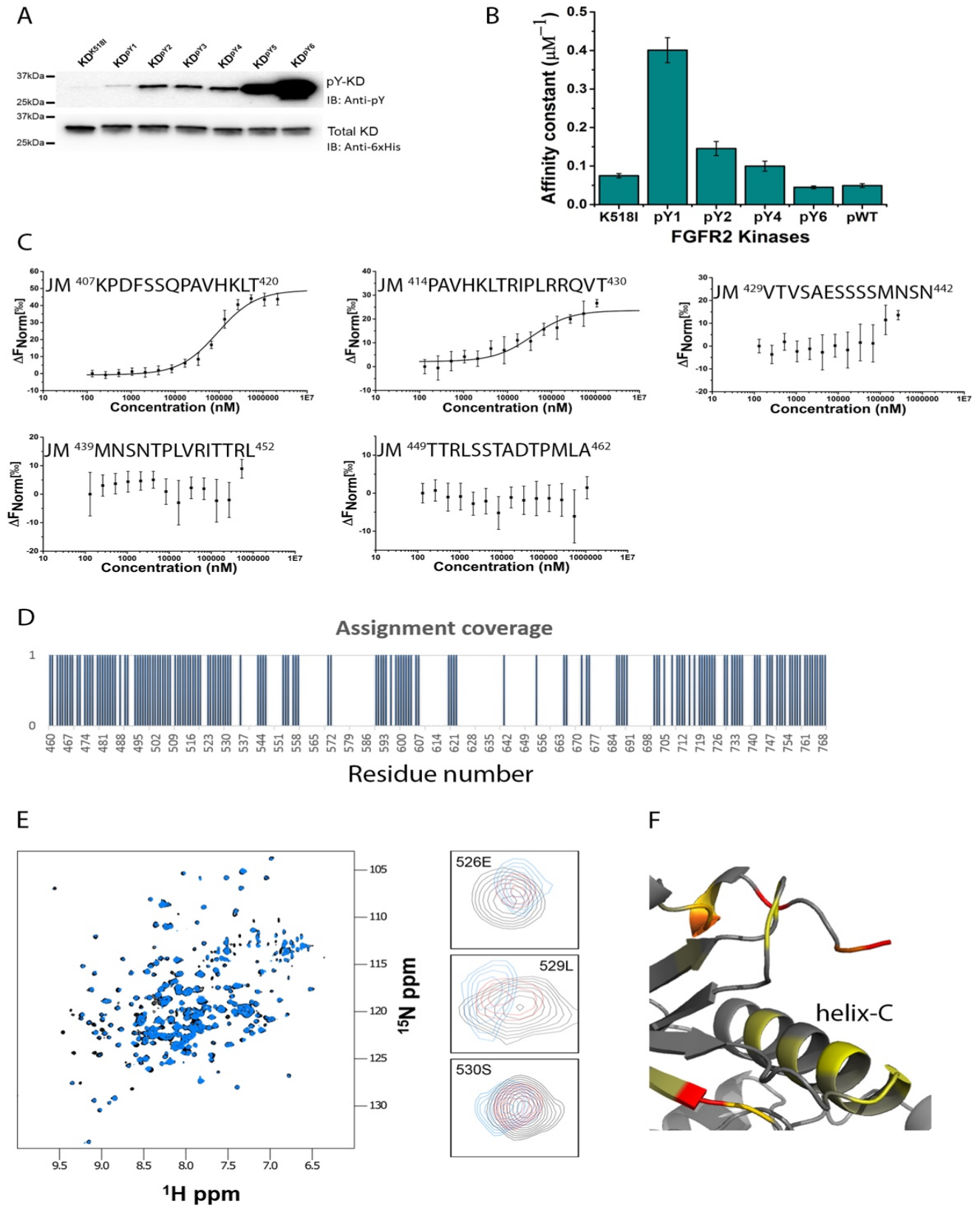9   *Corresponding author. Email: j.e.ladbury@leeds.ac.uk

10
11
12   This file includes:
13   Figs. S1 to S6
14   Tables S1 to S4

Supplemental Figure 1

Fig. S1. The interaction of JM to KD. (**A**) The phosphorylation states of KD^{pY1} to KD^{pY6} were confirmed using a phosphotyrosine pY99 antibody. An anti-6xHis tag antibody was used to probe for total proteins as the loading control. (**B**) Quantification of binding affinities between JM and KD with different phosphorylation states. The mono-phosphorylated KD is the strongest binding partner for JM. (**C**) Five short JM peptides were synthesised (residues 407-420, 414-430, 429-442, 439-452, and 449-462) and used to identify the binding region for KD^{pY1}. The MST measurement results indicate that residue 407-420 provides the best binding ability for KD^{pY1}. (**D**) Assignment coverage of KD amide backbones. Overall percentage of the assignment used in all titration experiment was 56% (not including prolines). (**E**) ^1H-^{15}N HSQC spectra of unbound mono-phosphorylated FGFR2 kinase KD^{pY1} (black) overlay with JM bound KD^{pY1} (blue) at 1:2 ratio. Examples of peaks with high chemical-shift perturbations (CSPs) are shown by labels indicating the assignment of given peaks. (**F**) CSPs of JM binding to KD^{pY1} plotted on the X-ray structure of mono-phosphorylated kinase. Minor CSPs appear on one side of the regulatory α-C helix, suggesting the binding of JM could regulate kinase activity. CSPs shown as gradient: Yellow – lower, Red - higher.

Supplemental Figure 2
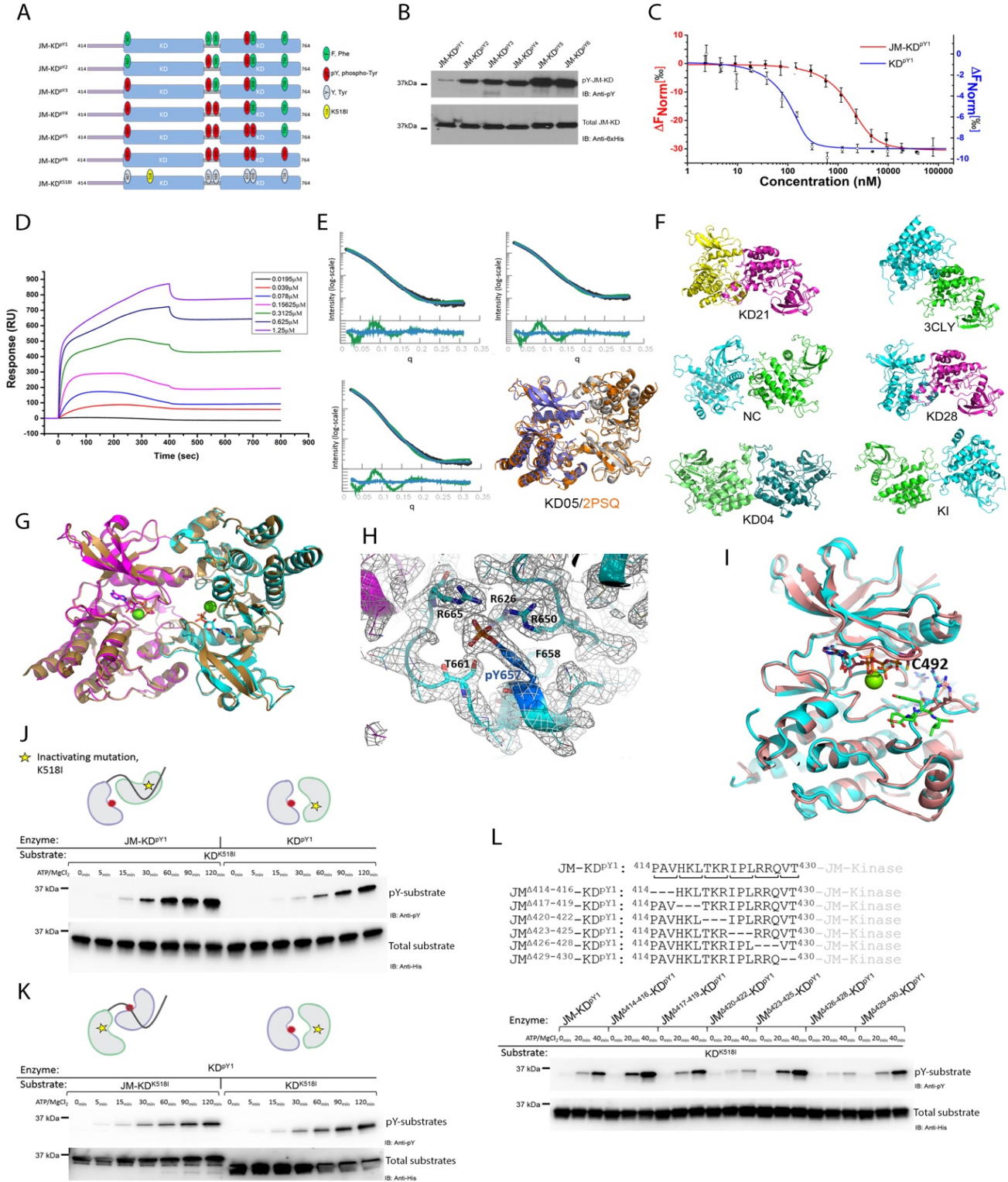
Fig. S2. Dimerization of mono-phosphorylated kinase. (**A**) Schematic of JM-KD with progressively phosphorylation KD (FGFR2$_{414\text{-}764}$). Six tyrosine residues on KD were mutated to mimic the sequential phosphorylation pattern of KD (JM-KD^{pY1} to JM-KD^{pY6}). (**B**) Phosphorylation states of JM-KD^{pY1} to JM-KD^{pY6} were examined using a phosphotyrosine pY99 antibody. An anti-6xHis tag antibody was used to probe for total proteins as the loading control. (**C**) The 'apparent' dimerization K$_d$ of JM-KD^{pY1} (red) and KD^{pY1} (blue) determined using MST. JM-KD^{pY1} and KD^{pY1}were labelled with Atto488 dye then titrated with unlabelled JM-KD^{pY1} and KD^{pY1}. (**D**) Dimerization of JM-KD^{pY1} was examined using surface plasmon resonance (SPR). JM-KD^{pY1} was immobilised on a CM4 chip by amine coupling, a serial dilution of JM-KD^{pY1} was injected for 400 seconds and washed with buffer for further 400 seconds. The binding affinity was calculated using steady-state fitting model. (**E**) SAXS description of the structure of KD^{pY1}. Top panel: the calculated SAXS pattern for 1-state (green) and 3-state (blue) models fitted to the experimental data (black) at different total maximum KD^{pY1} concentrations (top left plot, 65 µM; top right, 130 µM, and bottom 210 µM). For each scattering dataset the bottom panel shows the residuals of fit for 1-state (green) and 3-state models (blue). The resolution, q, is given in 1/Å and the intensity is given in arbitrary units. The structures in the bottom right panel show that the best-fitting crystal structure-derived (orange), and *in silico*-docked (blue/grey KD05) represent the same conformation. (**F**) Additional SAXS structures relevant to fitting of KD^{pY1} or JM-KD^{pY1} to SAXS data, reported in Fig. 2d, e and Table S3. (**G**) Phosphorylated chains A (magenta) and C (cyan) superimposed onto chains C and D (grey) together with both chains from the unphosphorylated FGFR2 kinase structure 2PSQ. ATP shown as a stick model and Mg^{2+} as green spheres. (**H**) A-loop (chain B) in its 2FoFc electron density. (**I**) Superimposition of KD^{pY1} (chain B) with 2PVF (salmon). (**J**) At the basal state, the presence of JM in the substrate-acting molecule (JM-KD^{K518I}) is required for the recruitment of kinase-acting molecule (KD^{pY1}). This asymmetric dimer configuration is required for the enhancement of transphosphorylation as the phosphorylation levels of substrates (left panel: JM-KD^{K518I}, right panel: KD^{K518I}) were examined using a phosphotyrosine antibody (pY99). An anti-6xHis tag antibody was used to probe total proteins as the loading control. (**K**) The JM from JM-KD^{pY1} cannot recruit and phosphorylate KD^{K518I}. figs. S2J and S2K demonstrate a role of kinase activation at basal state by which the JM interacts *in trans*, recruiting and phosphorylating a substrate molecule. (**L**) Deletion in the JM identifies the critical motifs, ^{420}TKR^{422} and ^{426}RRQ^{428}, for JM to recruit and phosphorylate substrate.

Supplemental Figure 3
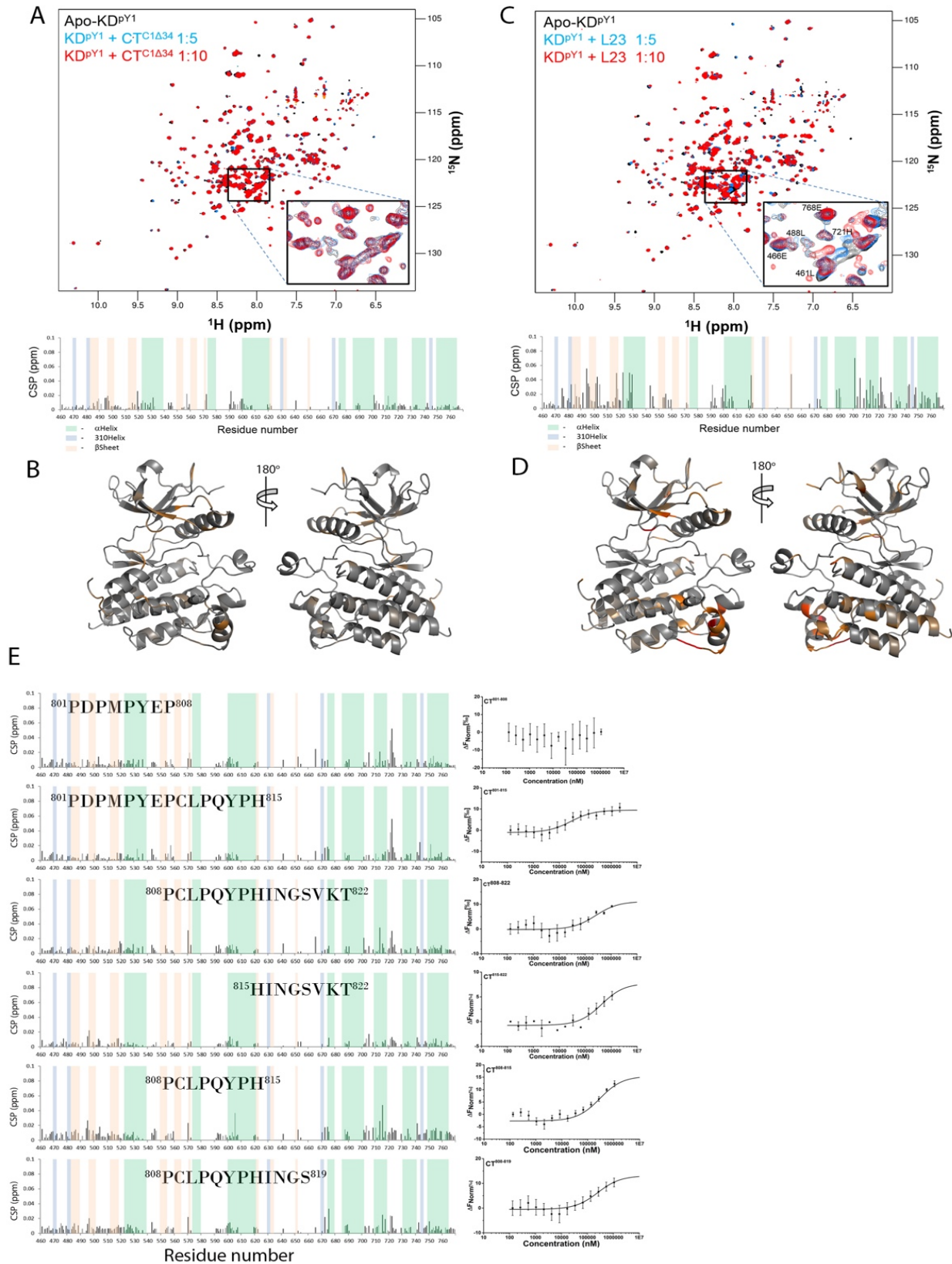
64   **Fig. S3. CT^{C1} fragments bind to KD^{pY1}.** (**A**) The first 24 residues (CT$^{C1\Delta34}$) of CT shows negligible
65   interaction with ^{15}N-labelled KD^{pY1}. There is no significant CSPs observed in the HSQC spectra and
66   calculated CSPs. (**B**) Mapping of the weak CSPs from CT$^{C1\Delta34}$ binding on the KD^{pY1} crystal structure. (**C**)
67   The last 23 residues (Last 23, L23) of CT shows major interaction with ^{15}N-labelled KD^{pY1}. Upon L23
68   binding, CSPs were observed in the HSQC spectra and calculated CSPs shows two clusters of residues
69   can respond to L23 peptide binding. (**D**) Mapping of the CSPs from L23 binding on the KD^{pY1} crystal
70   structure. (**E**) Using small CT peptides (801-808, 801-815, 808-822, 815-822, 808-815, and 808-819.
71   Sequences are shown in the Figure) for HSQC titration with ^{15}N-labelled KD^{pY1} in order to narrow down
72   sequence-specific binding region on kinase. The binding of each peptide to KD^{pY1} was also confirmed
73   using MST as shown on the right.
74
75
76
77
78
79
80
81
82
83
84
85
86
87
88

Supplemental Figure 4

A

89
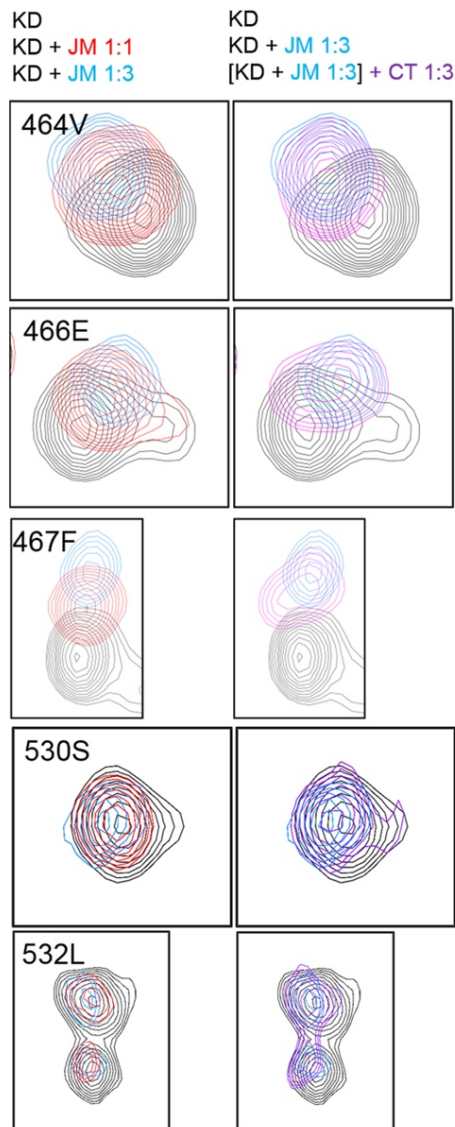
Fig. S4. Binding of CT does not compete with JM for binding to KD^{pY1}. (A) ^{15}N-labelled KD^{pY1} was titrated with 1:1 and 1:3 ratio of JM first. CSPs of selected residues were shown (the left hand panel. Apo, black; 1:1, red; 1:3, blue). The addition of 1:3 ratio of CT into the preformed JM-^{15}N-labelled KD^{pY1} shows the reduction of CSPs (Right panel; Apo, black; 1 x KD : 3 x JM, blue; [1 x KD : 3 x JM]+3 x CT, purple).

95

Supplemental Figure 5
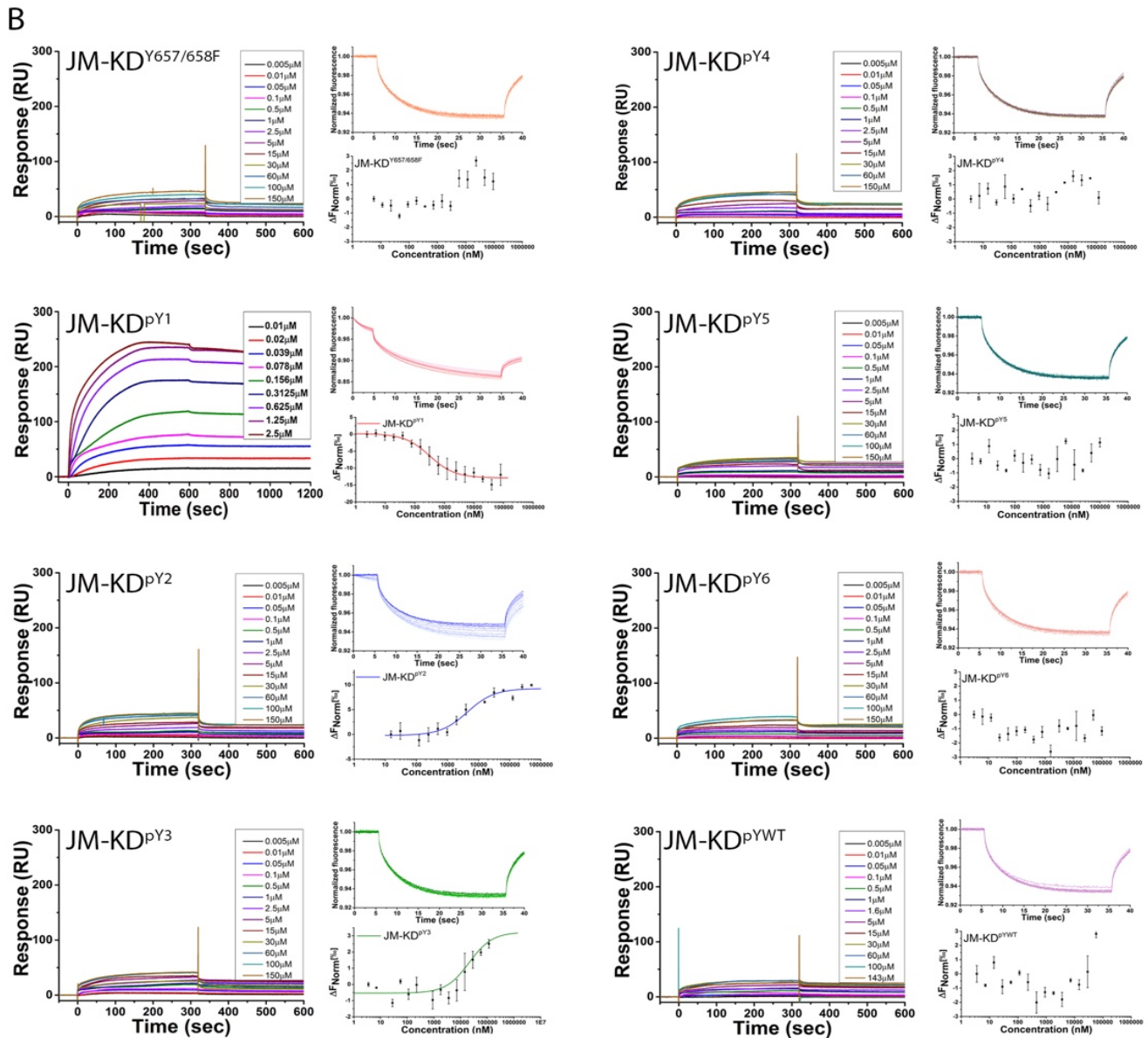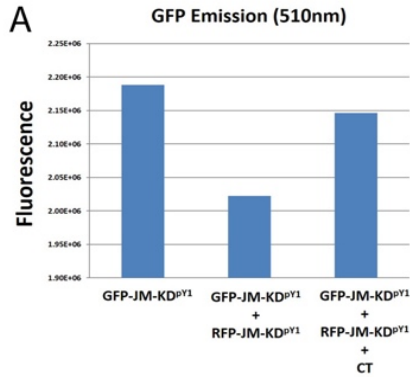
Fig. S5. Phosphorylation states control KD and CT^{C1} interaction. (**A**) Steady-state FRET study using GFP and RFP tagged JM-KD^{pY1} demonstrates that the dimer formation of GFP and RFP tagged JM-KD^{pY1} as indicated by the decrease of FRET donor emission (510nm). In addition, the binding of CT to JM-KD^{pY1} results in the dissociation of the asymmetric JM-KD^{pY1} dimer as indicated by the recovery of FRET donor emission (510nm). (**B**) The phosphorylation levels of JM-KD tightly control the interaction with CT. For the SPR experiments, untagged CT (the last 58 residues of FGFR2) was immobilised on a CM4 chip via amine coupling. Kinases with different phosphorylation level (JM-KD^{pY1} to JM-KD^{pY6}, and JM-KD^{pYWT}, and JM-KD$^{Y657/658F}$) were injected followed by a buffer wash. The binding affinities were determined using stead-state fitting. For the MST measurements, untagged CT was labelled by Atto 488. Two-fold serial dilutions of kinase proteins as described above were used to mix with labelled CT (100nM) and the binding affinities were determined. Both SPR and MST experiments show that the mono-phosphorylated JM-KD is the strongest binding partner for the CT. These experiments provide direct evidence of KD-CT interaction at the basal state.
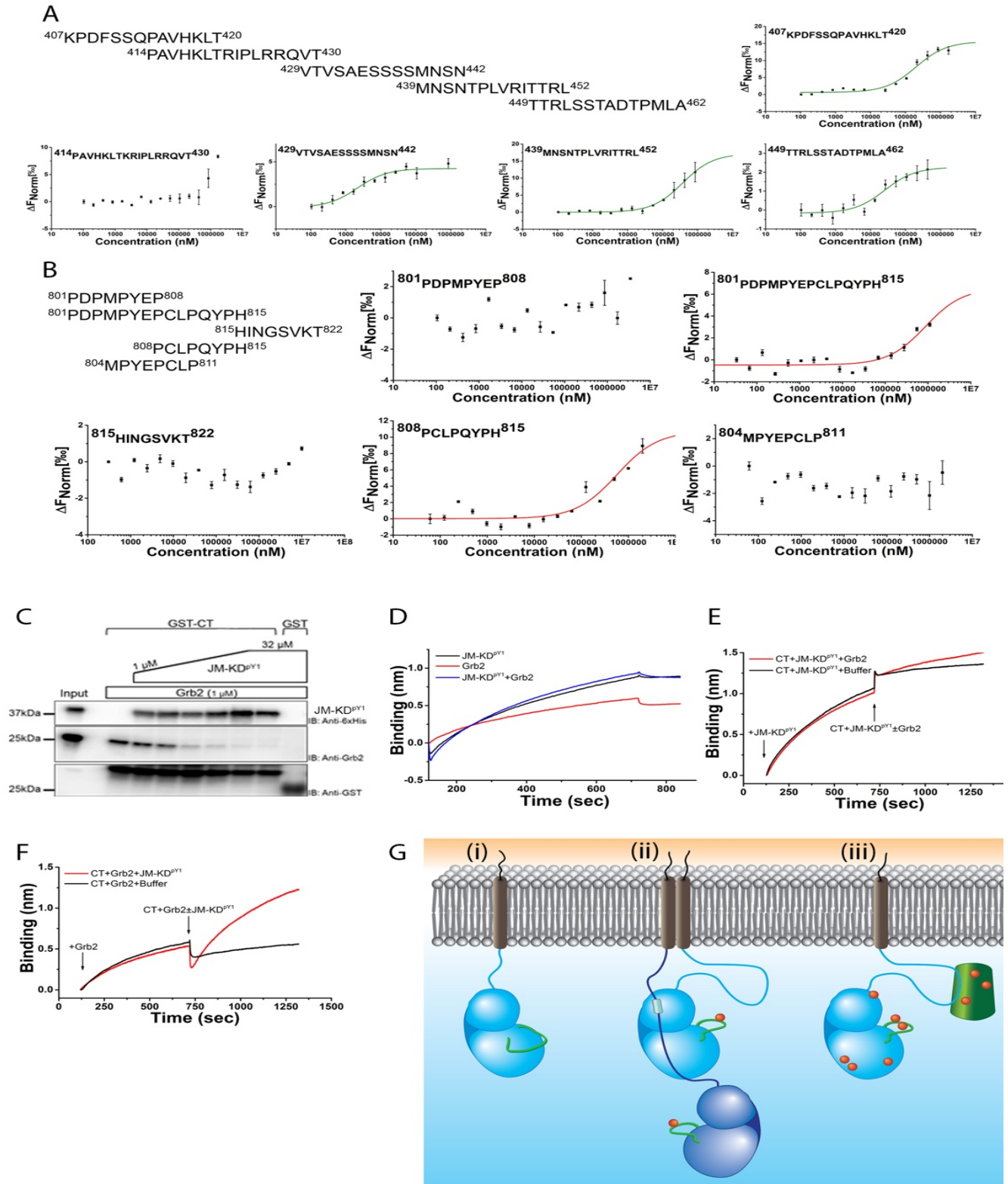
Supplemental Figure 6

115

Fig. S6. CT-JM interactions and CT competes with GRB2 for binding to JM-KD^{pY1}. (**A**) Small JM peptides (residues 407-420, 414-430, 429-442, 439-452, and 449-462) were used for the MST measurements with CT. CT was labelled with Atto 488 and 2-fold serial dilutions of small JM peptides were mixed with 100 nM labelled CT. (**B**) Small CT peptides (residues 801-808, 801-815, 815-822, 808-815, and 804-811) were used for the MST measurements with JM. JM was labelled with Atto488 and 2-fold serial dilutions of small CT peptides were mixed with 100 nM labelled JM. (**C**) GST-CT was used to pulldown GRB2 (1 µM) alone or GRB2 (1 µM) mixed with increased concentrations of JM-KD^{pY1} (1 µM to 32 µM). In the absence of JM-KD^{pY1}, GRB2 can be recruited to CT. However, binding of JM-KD^{pY1} to CT competes with GRB2 binding to CT as less Grb2 binds to CT in the presence of JM-KD^{pY1} in a concentration-dependent manner. (**D**) BLI sensors captured with CT show different binding behaviours upon 10µM of JM-KD^{pY1} (black) and GRB2 (red) binding. However, the binding curve for the JM-KD^{pY1}-GRB2 mixture shows similar curve (blue) to that of JM-KD^{pY1} alone (black), suggesting that in the presence of JM-KD^{pY1} GRB2 cannot bind to CT as the CT- JM-KD^{pY1} complex is preferable. (**E**) GRB2 does not compete with JM-KD^{pY1} for binding to CT. CT was captured on a BLI sensor and exposed JM-KD^{pY1} at 125 s (arrow) for 625 s, the level of bound JM-KD^{pY1} (10 µM solution in the sample well) on CT was shown as the increase of Binding signal (nm). After adding GRB2 (10 µM solution in the sample well) at 750 s as indicated by an arrow, no significant changes can be observed compared with buffer control (Grb2 addition, red; buffer addition, black). (**F**) JM-KD^{pY1} competes with GRB2 for binding to CT. CT was captured on a BLI sensor and exposed GRB2 at 125 s (arrow) for 625 s, the level of bound GRB2 (10 µM solution in the sample well) on the CT was shown as the increase of Binding signal (nm). After adding JM-KD^{pY1} (10 µM solution in the sample well) at 750 s as indicated by the arrow, a significant drop in the signal following by a graduate increase in signal compared with buffer control (JM-KD^{pY1} addition, red; buffer addition, black) indicating that JM-KD^{pY1} competes with GRB2 for binding to CT. (**G**) Schematic representation of activation of FGFR2^{C3} K*sam* mutant. i: In the absence of stimulation the unphosphorylated FGFR2^{C3} (light blue, JM light blue line) can exist as a monomer freely diffusing through the plasma membrane. ii: Under normal expression levels in non-stimulated cells FGFR2 will self-associate through random collision. Such collision between FGFR2^{C3} molecules in the absence of negative control of CT results in formation A-loop phosphorylation (red spot on green line) of JM latch and asymmetric dimerization to form active enzyme. (Enzyme-like receptor: dark blue, substrate-like receptor: light blue). iii) Active asymmetric dimerization leads to trans-autophosphorylation (red spots) of FGFR2^{C3} which is unrestrained by CT. The conformational change associated with phosphorylation of the KD enables recruitment and phosphorylation of FRS2 (green shape) and recruitment of downstream signalling effector proteins to initiate signal transduction.

162

Table S1. Biophysical measurements of FGFR2 JM, KD, and CT interactions.

FGFR2-derived polypeptides binding to JM (K_d) measured by MST	
KD^{K518I}	13.4±0.994 μM
KD^{pY1}	2.51±0.203 μM
KD^{pY2}	6.98±0.877μM
KD^{pY4}	10.2±1.33 μM
KD^{pY6}	22.5±1.8 μM
KD^{pWT}	20.5±2.04 μM
JM sequences binding to KD^{pY1} (K_d) measured by MST	
[407]juxtamembrane region[462]	2.51±0.203 μM
[407]KPDFSSQPAVHKLT[420]	105±7.37 μM
[414]PAVHKLTKRIPLRRQVT[430]	36.8±6.23 μM
[429]VTVSAESSSSMNSN[442]	> 1000 μM
[439]MNSNTPLVRITTRL[452]	No binding
[449]TTRLSSTADTPMLA[462]	No binding
CT sequences binding to KD^{pY1} (K_d) measured by MST	
[801]PDPMPYEP[808]	No binding
[801]PDPMPYEPCLPQYPH[815]	25.8±5.4 μM
[808]PCLPQYPHINGSVKT[822]	257±39.2 μM
[815]HINGSVKT[822]	426±42.5 μM
[808]PCLPQYPH[815]	291±21.4 μM
[808]PCLPQYPHINGS[819]	255±37.9 μM

FGFR2-derived polypeptides binding to CT^{C1} (μM) measured by SPR		SE(Kd)
JM-KD$^{Y657/658F}$	5.657E-3	1.9E-3
JM-KD^{pY1}	1.652E-4	1.6E-5
JM-KD^{pY2}	4.075E-3	5.2E-4
JM-KD^{pY3}	3.266E-3	8.2E-4
JM-KD^{pY4}	7.873E-3	1.7E-3
JM-KD^{pY5}	1.596E-3	2.0E-4
JM-KD^{pY6}	4.632E-3	9.1E-4
JM-KD^{pWT}	2.309E-3	4.8E-4
JM sequences binding to CT^{C1} (K_d) measured by MST		
[407]juxtamembrane region[462]	20.2±2.92 μM	
[407]KPDFSSQPAVHKLT[420]	200±13.7 μM	
[414]PAVHKLTKRIPLRRQVT[430]	No binding	
[429]VTVSAESSSSMNSN[442]	3.23±0.326 μM	
[439]MNSNTPLVRITTRL[452]	372±30.3 μM	
[449]TTRLSSTADTPMLA[462]	25.4±3.26 μM	
CT^{C1} sequences binding to JM (K_d) measured by MST		
[801]PDPMPYEP[808]	No binding	
[801]PDPMPYEPCLPQYPH[815]	63.6±6.5 μM	
[815]HINGSVKT[822]	No binding	
[808]PCLPQYPH[815]	56.6±5.5 μM	
[804]MPYEPCL^{P811}	No binding	

163

164

165

Table S2. Statistic parameters of SAXS experiments for KD^{pY1} and JM- KD^{pY1}.

KD^{pY1} conc \ multi	Single-state (χ^2 / model)	Two-state (χ^2 / models [weight])	Three-state (χ^2 / models [weight])
2.5 mg/ml	**2.24** / KD21 **12.71** / *2PSQ*	**2.13** / 2CLY [0.410]; mono [0.590] **4.21** / *2PSQ [0.307]; mono [0.693]* **3.94** / <u>KI3mer [0.105]; mono [0.895]</u>	**1.00** / KD05 [0.246]; KD04 [0.266]; mono [0.488] **1.35** / *2PSQ [0.305]; KI [0.171]; mono [0.524]* **1.29** / <u>2PSQ [0.203]; NC3mer [0.081]; mono [0.715]</u>
5.0 mg/ml	**4.18** / KD21 **36.12** / *2PSQ*	**4.92** / KD28 [0.613]; mono [0.387] **14.81** / *2PSQ [0.438]; mono [0.562]* **14.47** / <u>KI3mer [0.117]; mono [0.883]</u>	**1.76** / KD05 [0.311]; KD04 [0.294]; mono [0.396] **2.66** / *2PSQ [0.392]; KI [0.184]; mono [0.424]* **2.36** <u>/ 2PSQ [0.276]; NC3mer [0.088]; mono [0.635]</u>
8.0 mg/ml	**7.18** / CP21 **60.01** / *2PSQ*	**9.74** / CP28 [0.718]; mono [0.282] **25.63** / *2PSQ [0.492]; mono [0.508]* **26.11** <u>/ 2PSQ [0.492]; mono [0.508]</u>	**2.89** / CP05 [0.374]; CP04 [0.300]; mono [0.325] **4.71** / *2PSQ [0.463]; KI [0.184]; mono [0.352]* **4.26** / <u>2PSQ [0.339]; NC3mer [0.089]; mono [0.572]</u>
JM-KD^{pY1} conc \ multi	**Single-state (χ^2 / model)**	**Two-state (χ^2 / models [weight])**	**Three-state (χ^2 / models [weight])**
2.5 mg/ml	**15.30** / JM-KD13	**2.14** / 3CLY [0.154]; mono [0.846]	**1.40**/ JM-KD04 [0.219]; JM-KD03 [0.128]; mono [0.652]

| 5.0 mg/ml | **48.70** / JM-KD13 | **4.98** / 3CLY [0.153]; mono [0.847] | **2.48** / JM-KD04 [0.218]; JM-KD03 [0.125]; mono [0.658] |
| 8.0 mg/ml | **122.05** / JM-KD13 | **10.78** / 3CLY [0.141]; mono [0.859] | **3.04** / JM-KD04 [0.206]; JM-KD03 [0.111]; mono [0.684] |

Top: Analysis of KD^{pY1}. KD04: symmetric dimer, formed through C-lobes. KD05: a docked dimer arrangement corresponding to the dimer observed in PDB 2PSQ. KD21: compact asymmetric dimer from ClusPro2.0; the C-lobe of one kinase binds to N- and C-lobes of the receiver kinase. KD28: compact asymmetric dimer from ClusPro2.0; similar to CP21. 3CLY: asymmetric dimer based on PDB 3CLY (kinase C-tail phosphorylation). Mono: monomer, produced by Swiss-Model based on PDB 2PVF. NC3mer: trimer produced by combining a 2PSQ dimer with a NC dimer. KI3mer: trimer produced by combining a 2PSQ dimer with a KI dimer. The normal script, italics and underlining correspond to results based on using different pools as source for multimers. Normal script: using all monomeric and dimeric models, including in silico docked dimers and aggregates. Italics: using only monomeric and dimeric species present in crystal structures of FGFR1 1Y mutants. Underlined: using only monomeric, dimeric and trimeric species present in crystal structures of FGFR1 1Y mutants. For all Pools, the 3-state models fitted the experimental SAXS data significantly better than single or 2-state models (4-state models did not result in significant improvements and were not included), suggesting that at least 3 species co-exist in solution.

Bottom: Analysis of JM-KD^{pY1}. JM-KD03: two kinases are loosely connected through their juxtamembrane region. JM-KD04: asymmetric dimer, where the juxtamembrane region of the effector kinase latches onto the receiver kinase. JM-KD13: asymmetric dimer, where the juxtamembrane region of the effector kinase latches onto the receiver kinase. 3CLY: asymmetric dimer based on PDB id 3CLY (kinase C-tail phosphorylation). Mono: monomer, produced by Modeller based on PDB 2PVF. Model structures were selected from a pool including crystal structure-derived and *in silico*-docked dimeric and multimeric assemblies (55 different structures in total).

Table S3. X-ray data collection and refinement statistics.

Data collection	FGFR2IIIb (414-822), pY657 (PDB6V6Q)
Beam line	ALS 8.3.1
Wavelength (Å)	1.116
Space group	P 2$_1$ 2$_1$ 2$_1$

Cell dimensions	
a, b, c (Å)	64.0 86.5 254.2
Resolution (Å)	81.92 - 2.46 (2.55 - 2.46) [a]
R_{merge} (%)	9.8 (108.8) [a]
$I/\sigma(I)$	12.7 (1.8) [a]
$CC_{1/2}$	0.998 (0.326)
Completeness (%)	96.6 (80.3) [b]
Redundancy	6.7 (3.6) [a]
Refinement	
Resolution (Å)	81.92 - 2.46 (2.55 - 2.46) [a]
Number of reflections	50447 (5926)
R_{work}/R_{free} (%)	21.14/23.88
Number of atoms	
Protein	9,018
Ligands	124
Water	125
Average B factors (Å²)	
Protein	83.82
Ligands	49.06
Water	4
Rmsds	
Bond lengths (Å)	0.018
Bond angles (°)	0.098

192 Statistics for the highest-resolution shell are shown in parentheses.

193

194
195

Table S4. Proline mutants in RTK C-terminal tails and human cancers.

Receptor	Cancer	Mutation	Sequences
IGF1R	Cutaneous Melanoma	*P1304H*	PLDP
	Lung Squamous Cell Carcinoma	*P1290L*	PEP
	Uterine Endometrioid Carcinoma	*Q1344**	Truncation
InsR	Cutaneous Melanoma	*P1381S*	PRSNP
	Cutaneous Melanoma	*P1328T*	PLDR
	Glioblastoma Multiforme	*P1328S*	PLDR
c-kit	Mucinous Adenocarcinoma of the Colin and Rectum	*R946**	Truncation
CSF1R	Diffuse Type Stomach Adenocarcinoma	*P966L*	PLLQP
	Leiomyosarcoma	*P962S*	PLLQP
	Lung Adenocarcinoma	*E912**	Truncation
	Lung Squamous Cell Carcinoma	*Q911**	Truncation
PDGFRA	Glioblastoma Multiforme	*P1021L*	PLPDIDP
PDGFRB	Cutaneous Melanoma	*P1042S*	PLEGSP
	Cutaneous Melanoma	*P1042S*	PLEGSP
	Cutaneous Melanoma	*P1042L*	PLEGSP
	Cutaneous Melanoma	*P983Q*	SDHP
FLT4	Uterine Endometrioid Carcinoma	*E1294**	Truncation
VEGFR2	Endometrioid Carcinoma	*P1355A*	SSPP
	Uterine Endometrioid Carcinoma	*E1325**	Truncation
	Lung Adenocarcinoma	*E1323**	Truncation
	Hepatocellular Carcinoma	*Y1319**	Truncation
	Lung Squamous Cell Carcinoma	*P1280T*	PSFGGMVP
	Cutaneous Melanoma	*P1243S*	PSFGGMVP
	Cervical Squamous Cell Carcinoma	*R1229**	Truncation
	Rectal Adenocarcinoma	*R1229**	Truncation
	Bladder Urothelial Carcinoma	*Q1222**	Truncation
	Cutaneous Melanoma	*P1210S*	PKFH
	Prostate Adenocarcinoma	*Q1170**	Truncation
FGFR1	Cutaneous Melanoma	*E792**	Truncation
FGFR2	Prostate Adenocarcinoma	*P813T*	PQYP
	Cutaneous Melanoma	*P775L*	PLEQYS

	Uterine Endometrioid Carcinoma	*Y769**	Truncation
	Uterine Endometrioid Carcinoma	*Y769**	Truncation
FGFR4	Head and Neck Squamous Cell Carcinoma	*P788L*	PL**P**L
	Cutaneous Melanoma	*P763R*	**P**YSP
NTRK1	Cutaneous Melanoma	*P789T*	P**P**VY
ROR1	Cutaneous Melanoma	*P883H*	**P**LLP
	Cutaneous Melanoma	*P856Q*	PPPKSRS**P**
	Cutaneous Melanoma	*P826S*	PINGYPIP**P**
	Lung Adenocarcinoma	*P826L*	PINGYPIP**P**
	Cutaneous Melanoma	*P825S*	PINGYPI**P**P
	Cutaneous Melanoma	*P818S*	**P**INGYPIPP
	Uterine Endometrioid Carcinoma	*R815**	Truncation
	Uterine Mixed Endometrial Carcinoma	*R815**	Truncation
	Cutaneous Melanoma	*P811H*	PPI**P**
	Tubular Stomach Adenocarcinoma	*P808L*	**P**PIP
	Glioblastoma Multiforme	*P761H*	**P**SGG
ROR2	Head and Neck Squamous Cell Carcinoma	*P901T*	**P**EDG
	Cutaneous Melanoma	*P878L*	**P**SNT
	Esophageal Squamous Cell Carcinoma	*P853T*	PQQVP**P**QMVPKP
	Uterine Endometrioid Carcinoma	*P839L*	PNFY**P**VQIP
	Uterine Endometrioid Carcinoma	*P826L*	**P**VP
	Hepatocellular Carcinoma	*Q816**	Truncation
	Head and Neck Squamous Cell Carcinoma	*P813T*	RPMV**P**PP
	Cutaneous Melanoma	*P803L*	PQPQFIP
	Bladder Urothelial Carcinoma	*P794A*	A**P**PFPQPQ
	Lung Adenocarcinoma	*Y786**	Truncation
MET	Bladder Urothelial Carcinoma	*S1390**	Truncation
	Uterine Endometrioid Carcinoma	*R1382**	Truncation
	Cutaneous Melanoma	*P1366S*	PY**P**S
AXL	Cutaneous Melanoma	*P848S*	PPTQPD**P**
	Cutaneous Melanoma	*P848L*	PPTQPD**P**
c-MER	Stomach Adenocarcinoma	*W938**	Truncation

	Lung Squamous Cell Carcinoma	L858*	Truncation
TYRO3	Head and Neck Squamous Cell Carcinoma	Q866*	Truncation
	Papillary Thyroid Cancer	G854*	Truncation
	Cutaneous Melanoma	G816*	Truncation
	Breast Invasive Ductal Carcinoma	P813L	EEP
EphA1	Head and Neck Squamous Cell Carcinoma	Q955*	Truncation
	Head and Neck Squamous Cell Carcinoma	Y930*	Truncation
	Uterine Endometrioid Carcinoma	P914L	PSLS
EphA3	Lung Adenocarcinoma	P961R	PQKK
EphA4	Hepatocellular Carcinoma	P985H	MVPV
	Cutaneous Melanoma	Q948*	Truncation
EphA5	Lung Adenocarcinoma	P1036T	VPL
	Lung Adenocarcinoma	P1036L	VPL
	Uterine Endometrioid Carcinoma	E1025*	Truncation
	Cervical Squamous Cell Carcinoma	Q1024*	Truncation
	Lung Squamous Cell Carcinoma	E984*	Truncation
	Lung Squamous Cell Carcinoma	P961T	PLG
	Lung Squamous Cell Carcinoma	X951_splice	
	Cutaneous Melanoma	P939L	PSS
EphA6	Colon Adenocarcinoma	R1108*	
	Rectal Adenocarcinoma	P1052L	PESPGEVPEYP
	Diffuse Large B-Cell Lymphoma, NOS	P1052L	PESPGEVPEYP
	Stomach Adenocarcinoma	P1052L	PESPGEVPEYP
	Lung Squamous Cell Carcinoma	W1007*	Truncation
	Cutaneous Melanoma	P992S	PAPMGCP
	Lung Adenocarcinoma	P992L	PAPMGCP
	Uterine Serous Carcinoma/Uterine Papillary Serous Carcinoma	P992H	PAPMGCP
	Endocervical Adenocarcinoma	P970H	PYW
	Cutaneous Melanoma	E962*	Truncation
EphA7	Cutaneous Melanoma	P903S	PNSLKPT
	Cutaneous Melanoma	P903L	PNSLKPT
	Rectal Adenocarcinoma	R895*	Truncation

	Colon Adenocarcinoma	*R895**	Truncation
	Cutaneous Melanoma	*R895**	Truncation
	Uterine Endometrioid Carcinoma	*R895**	Truncation
	Uterine Endometrioid Carcinoma	*R895**	Truncation
	Uterine Endometrioid Carcinoma	*R895**	Truncation
	Uterine Endometrioid Carcinoma	*R895**	Truncation
	Uterine Endometrioid Carcinoma	*R895**	Truncation
EphB1	Uterine Endometrioid Carcinoma	*P898H*	PSQP
	Lung Adenocarcinoma	*P885A*	PAS
EphB3	Breast Invasive Ductal Carcinoma	*P995S*	PVQV
	Head and Neck Squamous Cell Carcinoma	*Q909**	Truncation
EphB4	Diffuse Type Stomach Adenocarcinoma	*P985T*	PAPQY
	Renal Clear Cell Carcinoma	*P985A*	PAPQY
	Cervical Squamous Cell Carcinoma	*P977L*	PGTP
EphB6	Lung Squamous Cell Carcinoma	*P942T*	PVALDFPCLDSP
RET	Pancreatic Adenocarcinoma	*P1070S*	PNWPGESPVP
	Cutaneous Melanoma	*P1049S*	PLPRALP
ROS1	Uterine Endometrioid Carcinoma	*P2260S*	IMP
LMTK1	Cutaneous Melanoma	*P1107S*	PVPLRS
	Cutaneous Melanoma	*P1086S*	PPEPQGP
	Cutaneous Melanoma	*P1086L*	PPEPQGP
	Renal Clear Cell Carcinoma	*P1011T*	PEK
	Lung Squamous Cell Carcinoma	*P960H*	PQA
	Cutaneous Melanoma	*P922S*	PSATGP
	Head and Neck Squamous Cell Carcinoma	*P888L*	PDVVP
	Papillary Renal Cell Carcinoma	*P808T*	PSQEGAPLP
	Lung Adenocarcinoma	*P709H*	PSPKQTPRASP EPGYPGEP
	Papillary Renal Cell Carcinoma	*P647T*	PAFFE DPLGTSP
	Cutaneous Melanoma	*P636S*	PAFFE DPLGTSP
	Colon Adenocarcinoma	*P337S*	PYP
LMTK2	Uterine Serous Carcinoma/Uterine Papillary Serous Carcinoma	*P1451A*	PPPP
	Cutaneous Melanoma	*P1427L*	PDPF

	Cutaneous Melanoma	*P1372T*	PTK
	Cutaneous Melanoma	*P1346H*	PDPLP
	Colon Adenocarcinoma	*P1317S*	PVPI
	Uterine Endometrioid Carcinoma	*P1180L*	PEP
	Cutaneous Melanoma	*P1069S*	PPNP
	Cutaneous Melanoma	*P887H*	PFPASEP
	Cutaneous Melanoma	*P842L*	PTCLDVIVP
	Cutaneous Melanoma	*P631T*	PESP
	Cutaneous Melanoma	*P519L*	PGPG
	Colon Adenocarcinoma	*P445L*	PIL
LMTK3	Breast Invasive Lobular Carcinoma	*P1457T*	PAGP
	Lung Squamous Cell Carcinoma	*P1438L*	PALETPGPPARAP
	Bladder Urothelial Carcinoma	*P1425T*	PLLPPPGPP
	Serous Ovarian Cancer	*P1424S*	PLLPPPGPP
	Renal Clear Cell Carcinoma	*P1093S*	RAP
	Colon Adenocarcinoma	*P1029S*	PGPWEKTP
	Head and Neck Squamous Cell Carcinoma	*P922S*	PSLSLP
	Papillary Renal Cell Carcinoma	*P917T*	PSLSLP
	Cervical Squamous Cell Carcinoma	*P845L*	PRPRAPPEPPDPGAPRPPPDPGPLPLPGPREKP
ALK	Serous Ovarian Cancer	*P1542Q*	PPNV
	Uterine Serous Carcinoma/Uterine Papillary Serous Carcinoma	*P1521S*	PTKKNNP
	Uterine Endometrioid Carcinoma	*P1521H*	PTKKNNP
	Colon Adenocarcinoma	*R1464**	Truncation
	Uterine Mixed Endometrial Carcinoma	*R1464**	Truncation
	Uterine Endometrioid Carcinoma	*R1464**	Truncation
	Cutaneous Melanoma	*P1398S*	PIEYGP
	Intestinal Type Stomach Adenocarcinoma	*P1398L*	PIEYGP
LTK	Lung Adenocarcinoma	*P846T*	PLGPWLSSGLKP
	Cutaneous Melanoma	*E800**	Truncation
STYK1	Head and Neck Squamous Cell Carcinoma	*P401L*	PELVVP
EGFR	Cutaneous Melanoma	*P1178L*	PKEAKP

	Mixed Germ Cell Tumor	*P1178L*	PKEAKP
	Uterine Endometrioid Carcinoma	*P1123S*	PLNPAPSRDPH YQDP
	Stomach Adenocarcinoma	*R1068**	Truncation
	Uterine Endometrioid Carcinoma	*R1068**	Truncation
	Lung Squamous Cell Carcinoma	*P1019L*	LIPQ
	Uterine Endometrioid Carcinoma	*Y1016**	Truncation
	Cutaneous Melanoma	*Q982**	Truncation
	Cutaneous Melanoma	*Q982**	Truncation
ErbB2	Esophageal Adenocarcinoma	*E1229**	Truncation
	Mucinous Adenocarcinoma of the Colon and Rectum	*P1227S*	PPERGAPP
	Glioblastoma Multiforme	*P1199T*	PEYLTPQGGAA PQPHPPPAFSP
	Bladder Urothelial Carcinoma	*P1156H*	PDVRPQPPSPR EGPLPAARP
ErbB3	Uterine Endometrioid Carcinoma	*P1326T*	PDYWH
	Cutaneous Melanoma	*Q1301**	Truncation
	Renal Clear Cell Carcinoma	*R1267**	Truncation
	Cutaneous Melanoma	*P1256Q*	PVPIMPTAGTTP
	Papillary Renal Cell Carcinoma	*P1247L*	PVPIMPTAGTTP
	Cutaneous Melanoma	*P1170L*	GTP
	Cutaneous Melanoma	*P1162Q*	PDTHLKGTP
	Cutaneous Melanoma	*E1098**	Truncation
ErbB4	Cervical Squamous Cell Carcinoma	*P1300L*	PGTVLPPPP
	Breast Invasive Ductal Carcinoma	*P1292S*	PGTVLPPPP
	Lung Squamous Cell Carcinoma	*E1283**	Truncation
	Cutaneous Melanoma	*P1282S*	PIVAENP
	Uterine Endometrioid Carcinoma	*E1280**	Truncation
	Uterine Endometrioid Carcinoma	*D1238**	Truncation
	Lung Adenocarcinoma	*P1206L*	PPKAEDEYVNEP
	Lung Adenocarcinoma	*Q1181**	Truncation
	Cutaneous Melanoma	*P1165L*	PMRDKPKQEYL NPVEENP
	Lung Adenocarcinoma	*E1148**	Truncation
	Head and Neck Squamous Cell Carcinoma	*P1137A*	PTVFAPERSP

	Intestinal Type Stomach Adenocarcinoma	*P1132S*	PTVFAPERSP
	Lung Adenocarcinoma	*Q1126**	Truncation
	Cutaneous Melanoma	*P1117L*	PVAP
	Mucinous Adenocarcinoma of the Colon and Rectum	*C1106**	Truncation
	Lung Squamous Cell Carcinoma	*P1092S*	PYRAPTSTIPEAP
	Uterine Endometrioid Carcinoma	*P1080S*	PYRAPTSTIPEAP
	Cutaneous Melanoma	*Q1063**	Truncation
	Renal Clear Cell Carcinoma	*P1054H*	PPPAYTP
	Cutaneous Melanoma	*P1053L*	PPPAYTP
	Leiomyosarcoma	*S1043**	Truncation
	Bladder Urothelial Carcinoma	*P1031L*	PQAFNIPPP
	Cutaneous Melanoma	*P998Q*	PSPN

196